

A more realistic representation of overshoot at the base of the solar convective envelope as seen by helioseismology

J. Christensen-Dalsgaard^{1,2*}, M.J.P.F.G. Monteiro^{3,4}, M. Rempel², M.J. Thompson^{2,5}

¹Danish Asteroseismology Centre, and Department of Physics and Astronomy, Aarhus University, Ny Munkegade, DK-8000 Aarhus C, Denmark

²High Altitude Observatory, NCAR†, Boulder CO 80307-3000, USA

³Centro de Astrofísica, Universidade do Porto, Rua das Estrelas, 4150-762 Porto, Portugal

⁴Departamento de Física e Astronomia, Faculdade de Ciências, Universidade do Porto, Portugal

⁵School of Mathematics & Statistics, University of Sheffield, Hounsfield Road, Sheffield S3 7RH, United Kingdom

Accepted ; Received ; in original form 2009 September 11

ABSTRACT

The stratification near the base of the Sun’s convective envelope is governed by processes of convective overshooting and element diffusion, and the region is widely believed to play a key role in the solar dynamo. The stratification in that region gives rise to a characteristic signal in the frequencies of solar p modes, which has been used to determine the depth of the solar convection zone and to investigate the extent of convective overshoot. Previous helioseismic investigations have shown that the Sun’s spherically symmetric stratification in this region is smoother than that in a standard solar model without overshooting, and have ruled out simple models incorporating overshooting, which extend the region of adiabatic stratification and have a more-or-less abrupt transition to subadiabatic stratification at the edge of the overshoot region. In this paper we consider physically motivated models which have a smooth transition in stratification bridging the region from the lower convection zone to the radiative interior beneath. We find that such a model is in better agreement with the helioseismic data than a standard solar model.

Key words: convection – Sun: helioseismology – Sun: interior – stars: interior

1 INTRODUCTION

An understanding of the overshoot region at the bottom of the Sun’s convective envelope is important for a number of reasons. The overshoot region approximately coincides with the solar tachocline, a region of rotational shear which is generally believed to play a key role in the solar dynamo: overshooting is likely to be important for helping to store the magnetic flux below the convection zone during the solar cycle. Bulk motion in the overshoot region also affects the thermal stratification and it may contribute to significant mixing of chemical elements, for example transporting fragile elements such as lithium to hotter regions where they are destroyed more easily than in the convection zone. More generally, convective overshoot in stars (particularly those with convective cores) is likely to be an important and as yet imperfectly understood process affecting age estimates of stars, and so improved constraints on theories of overshooting obtained from a study of how overshooting works in the solar case can be important for understanding stars more widely.

Helioseismology provides a means of probing directly the

conditions inside the Sun, because the frequencies of resonant modes set up by acoustic waves propagating in the solar interior depend in particular on the adiabatic sound speed c which is given by

$$c^2 = \frac{\Gamma_1 p}{\rho} \approx \frac{\Gamma_1 k_B T}{m_u \mu} . \quad (1)$$

Here Γ_1 is the logarithmic derivative of pressure p with respect to density ρ at constant specific entropy, T is temperature, μ is the mean molecular weight, k_B is Boltzmann’s constant and m_u is the atomic mass unit. Hence the sound-speed gradient with respect to depth depends on the temperature gradient, which itself depends on the mechanism by which heat is transported. The transition between fully radiative heat transport beneath the convection zone and convective heat transport within the convection zone is manifest in the temperature gradient and hence too in the sound-speed gradient. If the transition in sound-speed gradient takes place over a distance that is small compared with the vertical wavelength of the acoustic waves near the base of the convection zone, then the transition appears to the waves to be more-or-less sharp and this gives rise to an oscillatory signal in the mode frequencies ω : the form of the signal gives information about the location and nature of this “acoustic glitch” (Gough 2002a).

Monteiro et al. (1994) represented the effect of the base of the convection zone in terms of an additive contribution $\delta\omega_p$ to the

* E-mail: jcd@phys.au.dk; mario.monteiro@astro.up.pt; rempel@ucar.edu; mjt@ucar.edu

† The National Center for Atmospheric Research is operated by the University Corporation for Atmospheric Research under sponsorship of the National Science Foundation

frequencies, relative to those of a corresponding model in which the transition had been smoothed out. For low-degree modes (see Monteiro et al. 2000) a break in the first derivative of the sound speed gives rise to a contribution of the form

$$\delta\omega_p = A(\omega) \cos(2\omega\bar{\tau}_d + 2\phi_0), \quad (2)$$

while a break in the second derivative gives rise to a similar signal but with a sine term instead of a cosine, and with a different frequency dependence of $A(\omega)$. Here $\bar{\tau}_d$ is essentially the value of τ at the location of the acoustic glitch, where

$$\tau = \int_r^R \frac{dr'}{c} \quad (3)$$

is acoustic depth beneath the surface, r being the corresponding distance to the centre and R the surface radius of the Sun. Also, ϕ_0 is a phase introduced by the reflection of the mode at the turning points, depending in particular on the near-surface structure. The function $A(\omega)$ is an amplitude which depends on the sharpness and nature of the convection-zone base: the smoother the transition, the smaller in general will be the amplitude. However, if moderate-degree data are used, as in the case of Sun where we have accurate data for modes whose degree is above 3, the above expression needs to include additional terms, both in the amplitude (Monteiro et al. 1994) and in the argument of the signal (Christensen-Dalsgaard et al. 1995), to account for the first-order effect of the mode degree on the signal.

Overshoot at the base of the solar convection has traditionally been modelled using non-local mixing-length theory (e.g., Zahn 1991). Such models mostly predict an overshoot region that is nearly adiabatically stratified; in terms of the logarithmic temperature gradient $\nabla = d \ln T / d \ln p$ one finds that $\delta \equiv \nabla - \nabla_{\text{ad}} \sim -10^{-6}$, where $\nabla_{\text{ad}} = (\partial \ln T / \partial \ln p)_s$, is the adiabatic temperature gradient, s being specific entropy. The depth of overshoot region is typically between $0.2H_p$ and $0.4H_p$, where H_p is the pressure scale height at the base of the convection zone, with a very steep transition towards the radiative temperature gradient. The results have seemed rather robust, since the above behaviour is found in models incorporating quite different large-scale flow structures: for example van Ballegooyen (1982) assumed overturning convective rolls whilst Schmitt et al. (1984) explicitly modelled downward plumes in the overshoot region. We note, however, that other treatments of the overshoot region have suggested a much smoother transition to the radiative gradient (e.g., Xiong & Deng 2001; Deng & Xiong 2008; Baturin & Mironova 2010).

The rather abrupt transition in the temperature gradient predicted by the non-local mixing-length models has been parameterized and incorporated into solar models (Basu et al. 1994; Basu & Antia 1994; Monteiro et al. 1994; Roxburgh & Vorontsov 1994; Christensen-Dalsgaard et al. 1995) in order to compare the predicted acoustic-mode frequencies with those observed on the Sun. Models with and without overshooting all have an oscillatory signal in frequencies coming from the base of the adiabatically stratified region, but the amplitude of the signal in the frequencies in the overshoot models is greater than in models without overshooting.

When the observed and model frequencies are compared, it is found that the amplitude of $\delta\omega_p$ in the Sun is comparable with or smaller than that in models without overshooting, implying that the amount of overshooting of the kind predicted by these mixing-length models is very small. Monteiro et al. (1994) and Christensen-Dalsgaard et al. (1995) concluded that the extent of any such overshoot at the base of the convection zone was less than

one tenth of a pressure scale-height. A similar limit was found by Basu et al. (1994), while Roxburgh & Vorontsov (1994) obtained a somewhat weaker limit. Basu & Antia (1994) noted that the composition gradient caused by the inclusion of helium settling produced a sharper transition in the sound-speed gradient, even in models without overshoot, and hence a larger oscillatory signal. From these analyses it would appear that the transition in sound-speed gradient at the base of the solar convection zone is if anything smoother than in the non-overshoot models. A caveat is that what we purport to measure in the above studies is the spherically symmetric component of the structure: departures from sphericity, such as a latitudinal dependence to the shape of the base of the convection zone, could make the transition appear smoother than it is locally. The helioseismic evidence, however, is that the location of the base of the convection zone is independent of latitude (Monteiro & Thompson 1998; Basu & Antia 2001). Changes of the base of the convection zone on time scales shorter than the observation interval could also have a similar effect by introducing a time-averaging effect on the mode frequencies that would mimic a smoother transition. The importance of this effect is difficult to estimate, however, and depends strongly on the 3D nature of convection at the base of the envelope.

Overshoot has been addressed in the last two decades by a variety of 2D and 3D numerical simulations (Roxburgh & Simmons 1993; Hurlburt et al. 1994; Singh et al. 1995, 1998; Saikia et al. 2000; Brummell et al. 2002; Rogers & Glatzmaier 2005b,a). Whilst the non-local mixing-length models have clearly predicted an adiabatic overshoot region of a sizeable fraction of a pressure scale height and a rather sharp transition to the radiative zone beneath, the numerical simulations show a greater variety of possible behaviours. The work by Brummell et al. (2002) is currently one of the best resolved and most turbulent investigations: it shows strongly subadiabatic overshoot with very smooth transition towards the radiative temperature gradient. Most of the earlier 2D and 3D simulation were more in the laminar regime and found, depending on their parameters (mainly the stiffness of the subadiabatic layer), both nearly adiabatic overshoot and extended subadiabatic overshoot.

Rempel (2004) tried to understand the cause of the discrepancies in different overshoot treatments, which have been attributed either to over-simplifications in the mixing-length approach and related models or to the fact that numerical simulations are not in the correct parameter range. Using a semi-analytic plume model Rempel (2004) showed that the main differences result from different values of the energy flux used in these models (more exactly the energy flux divided by the filling factor of downflows, expressed by a dimensionless number $\Phi \equiv F / (f p \sqrt{p/\rho})$, with the energy flux F , the downflow filling factor f , pressure p and density ρ at the base of the convection zone). The value of Φ ranges from 10^{-10} (mixing-length models) to up to 10^{-2} (numerical simulations). The influence of the energy flux (lower energy flux leading to more adiabatic overshoot) was already indicated in the work of Brummell et al. (2002) and has been confirmed by Käpylä et al. (2007) by varying the energy flux over two orders of magnitude (with the caveat that lowering the energy flux in a numerical simulations typically decreases also the degree of turbulence). The main conclusion of the work of Rempel (2004) is that non-local mixing-length models and current numerical simulations mark two extremes in terms of the parameter Φ and the Sun might have a solution somewhere in between, however most likely closer to the mixing-length regime unless the downflow filling factor at the base of the convection zone is tiny. This leads to the possibility that solar overshoot has a strat-

ification close to adiabatic, but with a transition towards the radiative gradient that is smoother than found in non-local mixing-length models.

Accordingly, we have created a family of semi-analytic models that display a range of possible characteristics for the convection zone, which may give better agreement with the helioseismic observations than the old non-local mixing-length models. Moreover, helioseismology may determine which model provides the best fit to the actual stratification of the Sun; this may, we hope, teach us something about the physics of convection and convective overshooting in stellar interiors.

The goal of the present paper is to discuss these models and compare their seismic properties with those observed. Section 2 presents the characteristics of the semi-analytic overshoot model and its parameterization in our stellar structure calculations. In Section 3 we describe the seismological method we use to analyse the oscillation frequencies to establish the characteristics of the transition in structure near the base of the convective envelope, and we apply it to the analysis of solar data in Section 4. Section 5 describes the solar models used in this study and presents the analysis of the frequencies computed from those models. In Section 6 we synthesize the observational and model results and discuss our inferences, and we present our conclusions in Section 7.

2 A SIMPLE PARAMETERIZATION FOR OVERSHOOT

As summarized in the introduction a variety of overshoot models including simplified plume models (Rempel 2004), non-local convection models (e.g., Xiong & Deng 2001; Deng & Xiong 2008), and 3D simulations (e.g., Brummell et al. 2002) predict overshoot profiles that are substantially smoother than those obtained through non-local mixing-length models. While the physical reasons for the smoother transitions differ among these models, the resulting profiles show a large degree of similarity. For the purpose of the helioseismic investigation in this paper it is not essential to use exactly one of these models. Rather what is important is to realize that overshoot profiles smoother than those obtained by standard mixing-length theory are possible. Using the models of Rempel (2004) as guidance we find the following properties to be rather general for all profiles:

- (i) The overshoot profile matches smoothly with the radiative gradient beneath.
- (ii) In the overshoot region ∇ is in between ∇_{rad} and ∇_{ad} .
- (iii) The lower part of the convection zone is weakly subadiabatic.

In this investigation we use a parameterization which produces overshoot profiles possessing the above-mentioned properties. After finding the overshoot profile that is most consistent with helioseismic data we shall return to overshoot models and discuss potential implications.

The idea is to provide an analytical match to the behaviour obtained in the numerical simulations by Rempel (2004), constrained such that the temperature gradient and its first derivative are everywhere continuous. This is done by representing the actual temperature gradient as a function of r thus:

$$\nabla = \nabla_{\text{ad}} - \mathcal{F}_{\text{ovs}} \frac{2}{\beta + \exp(2\zeta)} \quad \text{for} \quad r \geq r_{\text{f}}, \quad (4)$$

where $\zeta = (r - r_{\text{f}})/d$. For $r < r_{\text{f}}$, the temperature gradient is ra-

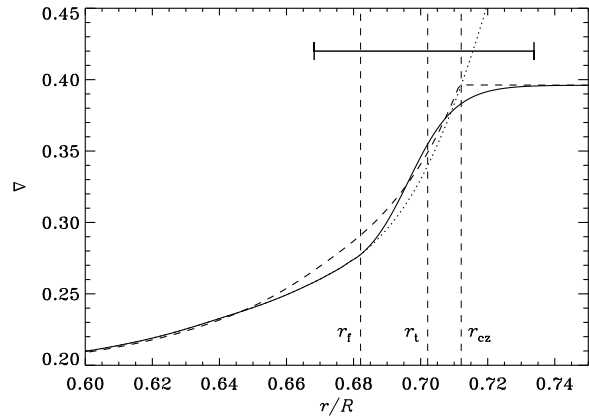


Figure 1. The temperature gradients ∇ (solid curve) and ∇_{rad} (dotted curve) in Model C2 with overshoot characterized by $r_{\text{cz}} - r_{\text{f}} = 0.01$, $r_{\text{t}} - r_{\text{f}} = 0.02$ and $\beta = 0.5$. The thin vertical dashed lines show the location of (from left to right) r_{f} , r_{t} and r_{cz} . For comparison, the dashed curve shows ∇ in Model S of Christensen-Dalsgaard et al. (1996), with no overshoot. The horizontal bar shows the range, around r_{t} , over which the argument ψ (cf. Eq. 8), at a frequency $\omega/2\pi = 2500 \mu\text{Hz}$, changes by π and hence provides a measure of the vertical wavelength of the acoustic waves.

diative, $\nabla = \nabla_{\text{rad}}$. The constants \mathcal{F}_{ovs} and d are determined such that

$$\left. \begin{aligned} \nabla &= \nabla_{\text{rad}} \\ \nabla' &= \nabla'_{\text{rad}} \end{aligned} \right\} \quad \text{at} \quad r = r_{\text{f}}, \quad (5)$$

where the dash indicates differentiation with respect to r . Thus the formulation is characterized by r_{t} , which determines the overall location of the transition from the adiabatic to radiative temperature gradient, and r_{f} , which is the radius at the bottom of the overshoot region, $r_{\text{t}} - r_{\text{f}}$ essentially controlling its width. We assume the full overshoot region, down to r_{f} , to be chemically fully mixed. The parameter β provides additional flexibility to the location of the overshoot region, relative to the base, $r = r_{\text{cz}}$, of the convectively unstable region, defined by $\nabla_{\text{rad}} = \nabla_{\text{ad}}$.

Given r_{t} , r_{f} and β , \mathcal{F}_{ovs} and d are determined from Eqs (5), which yield

$$\mathcal{F}_{\text{ovs}} = \frac{1}{2} \left[\nabla_{\text{ad}}(r_{\text{f}}) - \nabla_{\text{rad}}(r_{\text{f}}) \right] \left[\beta + \exp(2\zeta_{\text{f}}) \right], \quad (6)$$

where $\zeta_{\text{f}} \equiv (r_{\text{t}} - r_{\text{f}})/d$, and, neglecting ∇'_{ad} ,

$$\nabla'_{\text{rad}}(r_{\text{f}}) = -\frac{1}{d} \frac{2 \exp(2\zeta_{\text{f}})}{\beta + \exp(2\zeta_{\text{f}})} \left[\nabla_{\text{rad}}(r_{\text{f}}) - \nabla_{\text{ad}}(r_{\text{f}}) \right], \quad (7)$$

on using Eq. (6). Equation (7) can be solved for d and Eq. (6) then yields \mathcal{F}_{ovs} .

An example of the resulting ∇ is illustrated in Fig. 1, compared with the reference Model S with no overshoot. This clearly illustrates the region of subadiabatic stratification in the lower part of the convection zone, and the smooth match to the radiative gradient at the bottom of the overshoot region, in the model with overshoot. For comparison, the horizontal bar shows the wavelength of the squared vertical displacement eigenfunction ξ_r^2 (cf. Eq. 8) at a reference frequency $\omega/2\pi = 2500 \mu\text{Hz}$; it is evident that in both models the dominant transition takes place over a distance substantially smaller than the wavelength.

3 METHOD OF SEISMIC ANALYSIS

Following Monteiro et al. (1994) and Christensen-Dalsgaard et al. (1995), we consider the frequencies of the modes to be a sum of two components: a smooth component ω_0 , and an oscillatory component $\delta\omega_p$ coming from the acoustic glitch caused by the base of the convection zone and any overshoot.

The oscillatory signal arises because of the variation of the phase of the mode eigenfunctions at the location of the sharp feature, as a function of mode frequency and to a lesser extent of mode degree. Asymptotically, the radial displacement eigenfunction ξ_r is given by

$$\xi_r \propto (\rho c)^{-1/2} r^{-1} \cos[\psi(r)], \quad (8)$$

where

$$\psi(r) = \int_r^R \omega \left(1 - \frac{L^2 c^2}{\omega^2 r'^2} \right)^{1/2} \frac{dr'}{c} + \phi \quad (9)$$

and ϕ is a phase function (it is principally a function of frequency) which depends on conditions near the surface of the Sun: we discuss ϕ further below, and in detail in the Appendix.

As shown by Christensen-Dalsgaard et al. (1995), the acoustic glitch formed by the base of the convection zone and any region of overshooting gives rise to an oscillatory signal, with argument

$$\Lambda(\omega, l) \equiv 2\omega\bar{\tau}_d - \bar{\gamma}_d \frac{l(l+1)}{\omega} + 2\phi_0, \quad (10)$$

which can be expressed as

$$\begin{aligned} \delta\omega_p &= \frac{1-2\Delta}{(1-\Delta)^{5/2}} a_1 \left(\frac{\tilde{\omega}}{\omega} \right)^2 \sin[\Lambda(\omega, l)] \\ &+ \frac{1-2\Delta}{(1-\Delta)^2} a_2 \left(\frac{\tilde{\omega}}{\omega} \right) \cos[\Lambda(\omega, l)]. \end{aligned} \quad (11)$$

The second term is the form expected from a discontinuity in the first derivative of sound speed, and the first term from a discontinuity in the second derivative. Here

$$\Delta = \frac{l(l+1)}{\tilde{l}(\tilde{l}+1)} \left(\frac{\tilde{\omega}}{\omega} \right)^2 \Delta_d \quad (12)$$

(Δ_d is defined below) and \tilde{l} and $\tilde{\omega}$ are reference values of l and ω . For the present investigation we chose the reference values $\tilde{l}=20$ and $\tilde{\omega}/2\pi=2500 \mu\text{Hz}$.

To obtain Eq. (11) an expansion in Δ has been used to derive the expression for the amplitude: moreover, it has been assumed that the acoustic glitch is adequately represented by a single location r_d to perform the expansion in frequency.

The phase function ϕ , due to the reflection of the modes at the inner and outer turning points, is assumed to be represented asymptotically (Monteiro et al. 1994) by

$$\phi(\omega, l) \simeq \phi_0 + a_\phi \omega + a_\gamma \frac{l(l+1)}{2\omega}, \quad (13)$$

where (a_ϕ, a_γ) are unknown expansion coefficients. The remaining parameters are related to the internal structure of the star through the following relations:

$$\begin{aligned} \bar{\tau}_d &= \int_{r_d}^R \frac{dr}{c} + a_\phi, & \bar{\gamma}_d &= \int_{r_d}^R \frac{c}{r^2} dr + a_\gamma, \\ \Delta_d &= \frac{\tilde{l}(\tilde{l}+1)}{\tilde{\omega}^2} \left(\frac{c^2}{r^2} \right)_{r_d}, \end{aligned} \quad (14)$$

while a_1 and a_2 depend on the structure at the transition (see Christensen-Dalsgaard et al. 1995, for the details). Note that the

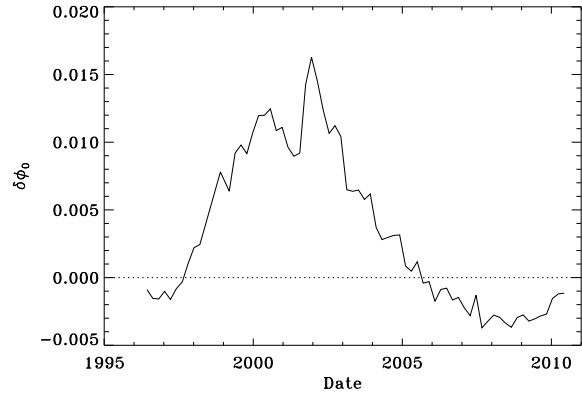


Figure 2. Difference in zero-frequency phase between the observations and Model S', obtained from differential asymptotic analysis (see Appendix A), plotted against the mean date of the observations.

measurable quantity $\bar{\tau}_d$ is not identical to τ_d , the acoustic depth of the acoustic glitch, because it includes a contribution a_ϕ from the dependence of ϕ on frequency. Similarly, $\bar{\gamma}_d$ contains a contribution from the l -dependent part of ϕ .

In the present work we are mainly interested in exploring the nature of the profile of the transition near the base of the convection zone. Thus we wish to measure the different contributions to the signal coming from the discontinuities in the first and second derivatives of the sound speed.

In previous works we have found that if ϕ_0 is also fitted as a free parameter, there is a strong correlation between the resulting values of $\bar{\tau}_d$ and ϕ_0 . This probably results from the fairly narrow range of frequencies included and the weak dependence on mode degree for most of the points, which means that a change in the average of $\omega\bar{\tau}_d$ can be compensated by a change in ϕ_0 and Δ_d . To overcome this difficulty the two terms in expression (11) were previously combined in a single cosine function with a single amplitude that depends on frequency and mode degree. However, this option weakens our capacity to study the actual behaviour of a_1 and a_2 for different profiles of the transition. Thus, in a departure from what we have done previously in Monteiro et al. (1994) and Christensen-Dalsgaard et al. (1995), here we use directly the expression (11) in the fit to the data to determine the four parameters ($a_1, a_2, \bar{\tau}_d, \bar{\gamma}_d$). The two components of the signal are fitted in the frequencies of modes with degrees $5 \leq l \leq 20$ and cyclic frequencies $1800 \leq \omega/2\pi \leq 4000 \mu\text{Hz}$ using an iterative least-squares procedure. The numerical approach is the same as described in Appendix C of Monteiro et al. (1994).

As noted above, if ϕ_0 is fitted as a free parameter it may be highly correlated with $\bar{\tau}_d$. However, as discussed in Appendix A, ϕ_0 can be determined independently from analysis of the oscillation frequencies and hence can be regarded as known in the fit to Eq. (11). We therefore adopt this procedure. There is still the difficulty of having Δ_d as free parameter of the fitting, due to the connection with $\bar{\gamma}_d$. Considering that Δ_d is a slowly varying function of τ in all models, we have chosen to adopt a reference value from the standard solar model corresponding to $\Delta_d = 0.35$.

In order to compare the amplitude of the signal for different models and the solar data it is convenient to use a reference value of the amplitude at fixed frequency $\tilde{\omega}$ and at $l = 0$ defined by

$$A_{2.5} = (a_1^2 + a_2^2)^{1/2}. \quad (15)$$

The principal quantities characterizing the signal due to the transition near the base of the convection zone are the period, measured by $\bar{\tau}_d$, and the amplitude (given by a_1 and a_2). The secondary quantities $\bar{\gamma}_d$ and Δ_d are necessary to account for the dependence on mode degree of the amplitude and the period of the signal (see Fig. 3 of Monteiro et al. 1994) as data up to $l = 20$ is used. The advantage of including the higher-degree data is that in general their frequencies are more precisely determined, and the much higher number of mode frequencies being used renders the fitting much more reliable.

Our least-squares fitting procedure weights all data equally, i.e., it does not take the quoted observational uncertainties into account. The reason for this choice is that we find it gives better determinations of the two amplitude parameters a_1 and a_2 : otherwise the largely systematic variation in mode frequency uncertainties with frequency causes these parameters to be less well constrained in the fitting. In practice it would correspond to putting all the weight on the low-frequency range of the spectrum. This would mainly lead to the determination of one of the a_i coefficients, rendering the other unnecessary in the fit. The solution would then be mostly determined by the initial guess. Such a frequency-dependent bias of the fitting can be removed if the fitting uses equal weights.

4 ANALYSIS OF SOLAR DATA

The solar data used in this work have been obtained from MDI/SOHO observations over a total period of over 14 years. To determine the signal we use sets of frequencies¹ obtained for 72 days of continuous observations (Schou 1999). Sets of frequencies for 1-year periods are also considered. These have been obtained by combining 5 consecutive sets of 72-d frequencies to produce an average for each 1-year set. Finally we considered frequencies from a coherently analysed set of 1-yr data from the beginning of the MDI observations. The results from this set were very similar to those of the corresponding 1-yr average of the 72-d sets and hence will not be discussed separately in the following.

We use modes having degree $5 \leq l \leq 20$ and cyclic frequency between 1900 and 4000 μHz . Because the least-squares fitting ignores the observational uncertainty on the frequencies, only modes with a quoted observational uncertainty below 0.1 μHz are used. The phase constant ϕ_0 was estimated as discussed in Appendix A, from a differential asymptotic analysis of each frequency set relative to the frequencies of Model S' that was adjusted to match approximately the solar frequencies. The resulting phase offset $\delta\phi_0$, as a function of the date of the observations, is illustrated in Fig. 2. In the analysis this offset is added to the phase $\phi_0 = 0.5485$ obtained for Model S' to obtain the appropriate phase constant for the particular observational dataset. The variation of $\delta\phi_0$ with phase in the solar cycle is discussed in Section A3.

To illustrate the quality of the fitting, Fig. 3 shows the signal $\delta\omega_p$ for the case of frequencies obtained from a 1-year time-series of observations from MDI. In order to show that our procedure has cleanly separated the smooth and oscillatory components of the frequencies, the lower panel shows the second differences of the ‘‘smooth’’ component of the frequencies, obtained after removing from the solar frequencies the fitted value of the signal at each frequency and mode degree. This illustrates that the

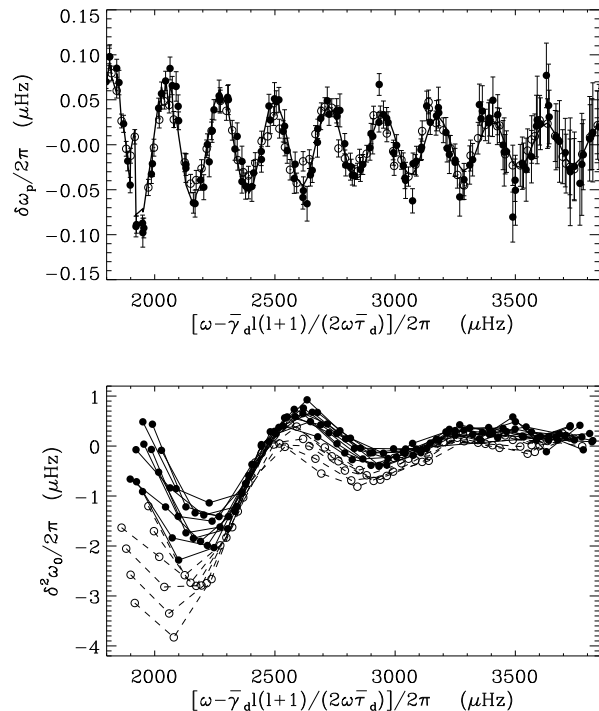


Figure 3. *Top panel:* Signal for a set of frequencies from MDI (1-year data), shown as filled circles for $5 \leq l \leq 14$ and open circles for $15 \leq l \leq 20$, with 1σ error bars. Also shown are the fitted values at each point from the expression in Eq. (11), using the parameters obtained by fitting the frequencies; to guide the eye, all points have been ordered by the reduced frequency used as abscissa and connected by a line. (The somewhat irregular behaviour arises from the dependence of the amplitude on ω and l .) *Bottom panel:* Second differences calculated for the smooth component ω_0 of the frequencies, obtained by subtracting from the frequencies the values represented by the line in the top panel. The lines connect points of the same mode degree (symbols as above).

signal coming from the base of the convection zone is no longer visible, while the signal due to the helium ionization zone (e.g. Monteiro & Thompson 2005) can be clearly seen in the second differences.

The impact of the observational uncertainties on $\bar{\tau}_d$, $A_{2.5}$ and the other measured parameters has been estimated in two ways. Firstly we compute the standard deviations of the measured values for a given parameter amongst all the 72-d observational datasets. Secondly, we make 500 Monte Carlo simulations of frequency datasets, using the estimated errors for a set of 72-d observational frequencies, fitting those artificial datasets in the same way as we fit the real data, and calculate standard deviations for the resulting estimated parameters. The estimate based on all the observed frequency sets will be affected by any temporal variations in the solar values, since the data are obtained at different epochs. The second estimate is purely an indicator of how the uncertainties in the frequencies impact the parameters measured from the signal. Both sets of uncertainties are shown in Table 1 together with the average values for the Sun. It is evident that the standard deviations in the parameters inferred from the observations are largely consistent with the result of the Monte Carlo simulation. Thus the scatter in the inferred values for $A_{2.5}$ for the observations is essentially consistent with the assumed error in the observed frequencies.

Figure 4 shows the inferred amplitude $A_{2.5}$ and period $\bar{\tau}_d$ for

¹ The frequencies are obtainable online courtesy of J. Schou at <http://quake.stanford.edu/~schou/anavw72z/>.

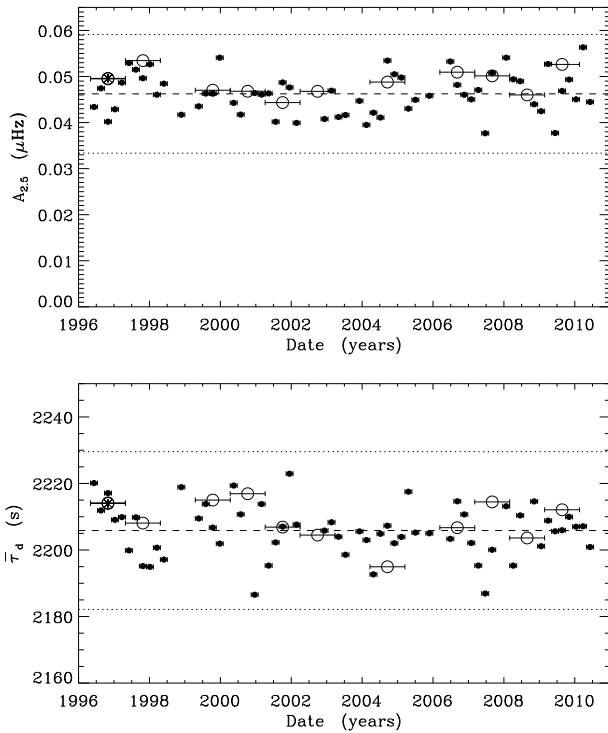


Figure 4. Values of the amplitude $A_{2.5}$ (top panel) and acoustic depth $\bar{\tau}_d$ (bottom panel) of the signal for sets of 72 days of MDI frequencies (full circles) and for sets of 1-year MDI frequencies (open circles), plotted against the mean date of the observations. The horizontal error bar represents the period of the time-series used for the calculation of the frequencies. The horizontal dashed line corresponds to the mean, and the horizontal dotted lines indicate $\pm 3\sigma$ standard deviations obtained by Monte Carlo simulations based on 72-d uncertainties of the solar frequencies.

Table 1. Seismic parameters (averages) resulting from the fit of the signal in Eq. (11) to the solar frequencies. Data sets for 72 days have been considered, as well as a coherently analyzed 360-d data set together with 1-year averages of 5 consecutive sets of 72-d frequencies. The values σ_{obs} are obtained as the 1σ distribution of the values found for each group of sets of solar frequencies (72-d and 360-d) while σ_{MC} are the 1σ of the Monte Carlo simulation (500 realizations) for a single set of frequencies using the quoted observational uncertainties in the frequencies for one of the 72-d sets and for one of the 1-year sets.

Type	$A_{2.5}$ (μHz)	a_1 (μHz)	a_2 (μHz)	$\bar{\tau}_d$ (s)	$\bar{\gamma}_d$ (μHz)
$\langle 72\text{-d} \rangle$	0.0462	0.0442	0.0101	2206	16.7
$\sigma_{\text{obs},72}$	0.0045	0.0045	0.0088	8	2.3
$\langle 360\text{-d} \rangle$	0.0488	0.0471	0.0095	2209	17.5
$\sigma_{\text{obs},360}$	0.0027	0.0042	0.0079	7	1.4
$\sigma_{\text{MC},72}$	0.0043	0.0045	0.0087	8	2.1
$\sigma_{\text{MC},360}$	0.0019	0.0018	0.0010	2	0.8

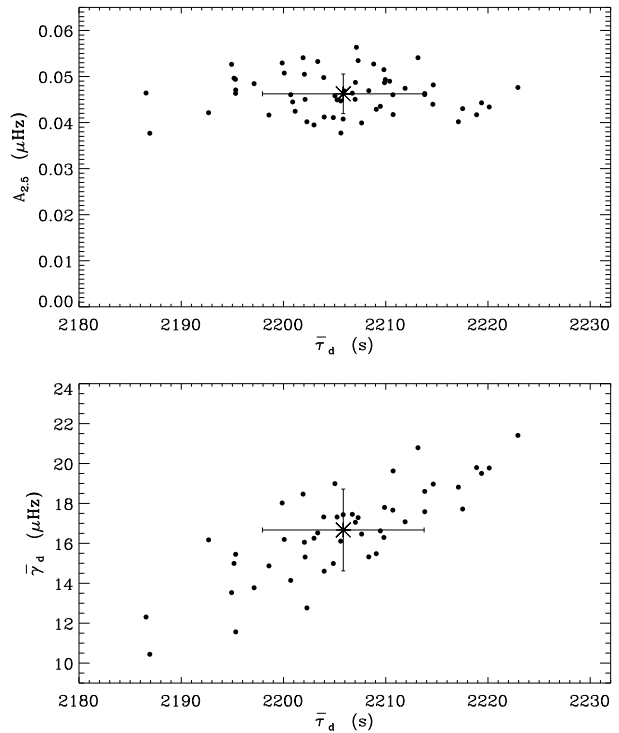


Figure 5. The filled circles are the values of $A_{2.5}$ (upper panel) and $\bar{\gamma}_d$ (lower panel), versus $\bar{\tau}_d$, for the solar data (72-d frequency sets). Also shown, as stars, are the average values of these values together with the error bars corresponding to a 1σ uncertainty estimated from Monte Carlo simulations for the uncertainties of a 72-d set of solar frequencies (see Table 1).

the solar data, as functions of epoch. The dashed lines indicate the average values over the whole period, and the dotted lines indicate the 3σ error interval obtained from Monte Carlo simulations based on the errors in the 72-d datasets. When 1-year data are used (see Table 1), there is some indication that the variation in the Sun in $\bar{\tau}_d$ and $\bar{\gamma}_d$ is slightly above the noise of the data. This could point towards a variation in time of the stratification of the overshoot region or the near-surface layers; there is indeed perhaps some hint of an orderly systematic variation of the 1-yr results in Fig. 4. (although not at an 11-yr period), but more accurate data would be necessary to confirm this possibility.

As a further indication of the properties of the parameters inferred from the 72-d datasets, Fig. 5 shows $A_{2.5}$ and $\bar{\gamma}_d$ against $\bar{\tau}_d$. While $A_{2.5}$ and $\bar{\tau}_d$ show no obvious correlation, there is a clear correlation between $\bar{\tau}_d$ and $\bar{\gamma}_d$. In fact it may be seen from Eq. (11) that both $\bar{\tau}_d$ and $\bar{\gamma}_d$ affect the phase of the signal, in such a way that an increase in $\bar{\tau}_d$ can be compensated by an increase in $\bar{\gamma}_d$, as observed in the lower panel of Fig. 5. This correlation is also confirmed by Monte Carlo simulations carried out on the basis of the model frequencies (see below). For other pairs of parameters no significant correlation was found.

5 ANALYSIS OF SOLAR MODELS

The signal for the models has been fitted using the same range of mode degree and frequency as done for the Sun (see above). In this way we have ensured that the fitting takes place under the same

conditions as for the solar data, both for error free data and for the Monte Carlo simulations used to estimate the impact of noise.

5.1 Models emulating overshoot

Apart from the treatment of the overshoot region, the models considered here were computed in the same way as Model S of Christensen-Dalsgaard et al. (1996). The computation used the OPAL equation of state (Rogers et al. 1996) and opacity (Iglesias et al. 1992), the Bahcall & Pinsonneault (1995) nuclear reaction rates, and the Michaud & Proffitt (1993) treatment of diffusion and settling of helium and heavy elements, the latter being treated as fully ionized oxygen. All models were calibrated, to within a relative accuracy of 10^{-6} , to a photospheric radius of 6.9599×10^{10} cm, a surface luminosity of 3.846×10^{33} erg s $^{-1}$ and a ratio $Z_s/X_s = 0.0245$ between the surface abundances by mass of heavy elements and hydrogen, at a model age of 4.6 Gyr. Further details on the model and oscillation calculations were given by Christensen-Dalsgaard (2008a,b).

To explore the sensitivity of the oscillations to the structure of the overshoot region we have considered a range of models with various characteristics, including models exhibiting the ‘classical’ sharp overshoot profile, a sequence of models converging towards the reference model, as well as models exhibiting various degrees of smoothness in the transition of the temperature gradient. Properties of the models are provided in Table 2. In discussing the models with overshoot or otherwise modified, we use Model S as reference.

Although the properties of the overshoot region are described in terms of the temperature stratification, the effect on the oscillation frequencies is predominantly controlled by the sound speed which in addition is affected by the composition. Of particular importance is the relatively steep gradient in the hydrogen abundance (X) established just below the fully mixed region which, as mentioned above, includes the overshoot region down to $r = r_f$. This affects the sound-speed gradient

$$\nabla_{c^2} \equiv \frac{d \ln c^2}{d \ln p} \simeq \nabla - \frac{d \ln \mu}{d \ln p}, \quad (16)$$

where the last approximation used Eq. (1). This behaviour is illustrated in Fig. 6. It is evident that the gradient in X accentuates the gradient in c^2 in Model S without overshoot (e.g., Basu & Antia 1994), and similarly produces a step in ∇_{c^2} at the edge of the overshoot region in Model C2 illustrated in the figure.

One might argue that further motion beyond the overshoot region would cause additional diffusive mixing, thus likely smoothing out the step in the sound-speed gradient. To investigate the effect of this on the signal we have computed Model OD, corresponding to Model C2 but with additional diffusive mixing in a small region beneath r_f ; specifically, the maximum diffusion coefficient, at the edge of the overshoot region, was $50 \text{ cm}^2/\text{s}$, decreasing rapidly with depth. This causes a modest smoothing of the hydrogen profile which evidently is sufficient to eliminate the step in ∇_{c^2} .

As a further background for the discussion of the model signals below, we first present a range of examples of profiles of the sound-speed gradient obtained with the formalism described in Section 2. These were chosen to provide an impression of the sensitivity of the signal to the detailed structure near the base of the convection zone, as well as to illustrate the structure that may be consistent with the observations. The input parameters of the models, and some relevant characteristics, are listed in Table 2. Here, τ_{cz} is the acoustic depth of the boundary r_{cz} of the convectively unstable region, while τ_{\max} is the acoustic depth of the point of steepest

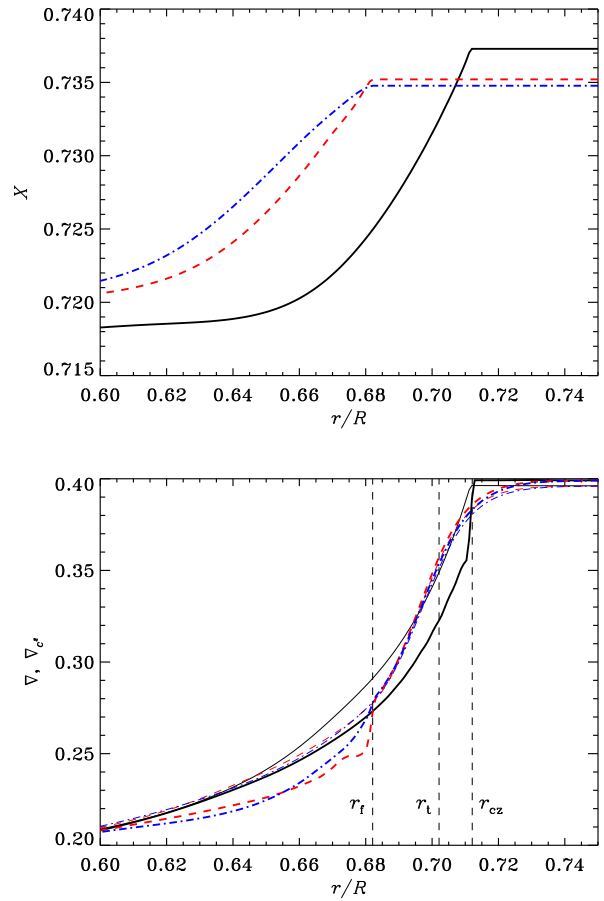


Figure 6. Properties of reference Model S (black solid lines), overshoot Model C2 (red dashed lines) and Model OD (blue dot-dashed line) which in addition has turbulent diffusion below the overshoot region. *Top panel:* Hydrogen abundance X against fractional radius r/R . *Bottom panel:* The thin curves show the temperature gradient $\nabla = d \ln T / d \ln p$, and the heavier curves the corresponding gradient in the squared sound speed (cf. Eq. 16). As in Fig. 1 the vertical dashed lines mark the location of r_f , r_t and r_{cz} in Model C2.

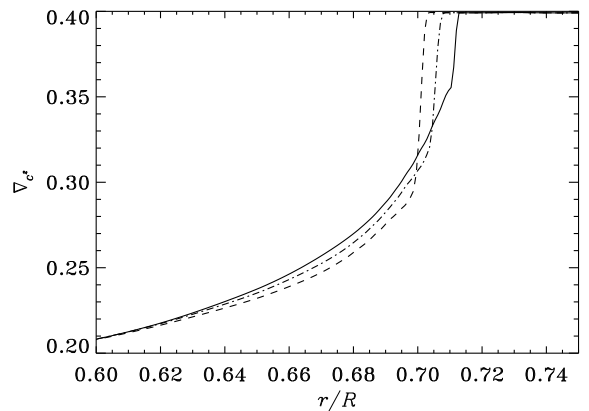


Figure 7. Gradients ∇_{c^2} of the squared sound speed in the reference Model S (solid line) and Models A1 (dashed line) and A2 (dot-dashed line) with a sharp transition at the bottom of the overshoot region.

Table 2. Model properties. Here S refers to Model S of Christensen-Dalsgaard et al. (1996), S' to a similar model, but with modified γ_1 in the near-surface layers (cf. Eq. A10), and models A1 – C3 were obtained utilizing the overshoot formulation described in Section 2, and characterized by r_t , r_f and β , r_{cz} and τ_{cz} being the radius and acoustic depth at the base of the convection zone, defined by $\nabla_{\text{rad}} = \nabla_{\text{ad}}$. Model OD in addition had a modest amount of turbulent mixing beneath the overshoot region while in Model OP the opacity near the boundary of the unstable region was reduced slightly (see text). To characterize further the properties of the models, τ_{max} shows the acoustic depth at the maximum in the overshoot region of $d\nabla/dr$, and ℓ_{ov}/H_p is the total extent $r_{cz} - r_f$ of the overshoot region, in units of the pressure scale height H_p at the base of the convection zone. Finally, ϕ_0 is the phase at zero frequency, determined from a fit to the eigenfunctions (cf. Appendix A).

Model	$\frac{r_{cz}-r_t}{R}$	$\frac{r_t-r_f}{R}$	β	τ_{cz} (s)	τ_{max} (s)	$\frac{\ell_{\text{ov}}}{H_p}$	ϕ_0
S	-	-	-	2171	2176	-	0.8904
S'	-	-	-	2176	2181	-	0.5485
A1	0.01	0.001	1.0	2170	2204	0.14	0.8916
A2	0.005	0.001	1.0	2171	2189	0.07	0.8914
B1	0.01	0.005	1.0	2170	2203	0.19	0.8898
B2	0.005	0.0025	1.0	2170	2188	0.09	0.8902
B3	0.0025	0.0010	1.0	2171	2181	0.04	0.8903
C1	0.01	0.015	0.5	2168	2212	0.31	0.8938
C2	0.01	0.02	0.5	2170	2217	0.37	0.8944
C3	0.01	0.025	0.5	2170	2219	0.44	0.8951
OD	0.01	0.02	0.5	2167	2217	0.37	0.8957
OP	0.02	0.02	1.0	2164	2227	0.50	0.8954

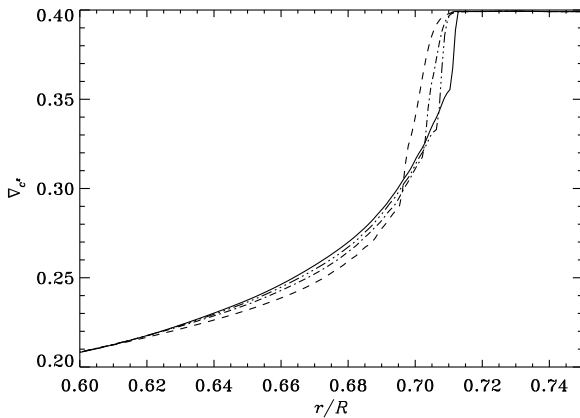


Figure 8. Gradients ∇_{c^2} of the squared sound speed in the reference Model S (solid line) and Models B1 (dashed line), B2 (dot-dashed line) and B3 (triple-dot-dashed line) converging to Model S (see also Table 2).

gradient in ∇ , providing an indication of the location of the acoustic glitch. Also, ϕ_0 is the extrapolated near-surface phase at zero frequency, determined from a fit to the eigenfunctions (see Section A1). Finally, for comparison with the common characterization of overshoot, ℓ_{ov}/H_p shows the overshoot distance $r_{cz} - r_f$, in units of the pressure scale height at r_{cz} . The properties of the models are illustrated in Figs 7 – 10 in terms of ∇_{c^2} .

Figure 7 shows that the present formulation emulates the sharp transition predicted by non-local mixing-length theories (e.g., Zahn 1991), and discussed in earlier work (Basu et al. 1994; Basu & Antia 1994; Monteiro et al. 1994; Roxburgh & Vorontsov 1994; Christensen-Dalsgaard et al. 1995) which provided stringent constraints on overshoot of this form. Figure 8 shows a sequence of models converging to Model S (see also the parameters in Table 2). A sequence of models of gradually increasing smoothness is illustrated in Fig. 9. Finally, Fig. 10 shows a model with a very smooth

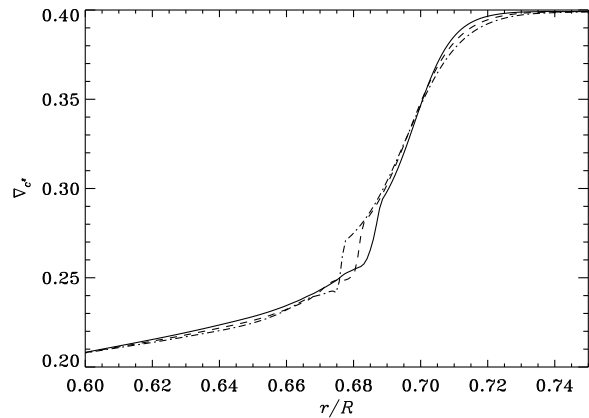


Figure 9. Gradients ∇_{c^2} of the squared sound speed in Models C1 (solid line), C2 (dashed line) and C3 (dot-dashed line), illustrating increasingly smooth overshoot.

transition. To ensure a reasonable sound-speed profile, in view of the helioseismic inference (see also Section 6.1), we shifted the boundary r_{cz} of the unstable region outwards by about $0.002R$ relative to Model S, through a localized reduction of the opacity by 7 per cent, centred near the bottom of the convective envelope.

The frequencies of all models have been fitted with Eq. (11) in order to obtain the four parameters (a_1 , a_2 , $\bar{\tau}_d$, $\bar{\gamma}_d$). Over 235 frequencies for each model have been used in the fit and no noise has been added to the frequencies. The values of the parameters found are listed in the first columns of Table 3.

The values for $A_{2.5}$ (see Eq. 15) were obtained from the fitted parameters a_1 and a_2 which, though not listed in the table, are illustrated in Fig. 11. The amplitude values depend mainly on the local conditions at the base of the convection zone and are insensitive to changes in the model that do not affect this layer. Therefore the distribution of the models in Fig. 11 is an accurate representation of the sharpness of the transition at the base of the envelope. We note

Table 3. Seismic parameters resulting from the fit of the signal in Eq. (11) to the frequencies of models. The first three columns are the results for noise-free data while the other six columns provide the results for 500 Monte Carlo simulations of each model when the uncertainties from a solar 72-d set of frequencies are considered.

Model	$A_{2.5}$ (μHz)	$\bar{\tau}_d$ (s)	$\bar{\gamma}_d$ (μHz)	$\langle A_{2.5} \rangle$ (μHz)	$\sigma(A_{2.5})$ (μHz)	$\langle \bar{\tau}_d \rangle$ (s)	$\sigma(\bar{\tau}_d)$ (s)	$\langle \bar{\gamma}_d \rangle$ (μHz)	$\sigma(\bar{\gamma}_d)$ (μHz)
S	0.0673	2164	13.1	0.0615	0.0043	2171	6	16.1	1.7
A1	0.1036	2184	13.5	0.0887	0.0046	2189	5	16.1	1.5
A2	0.0872	2173	13.4	0.0767	0.0043	2180	5	16.2	1.5
B1	0.0950	2185	13.6	0.0824	0.0048	2191	5	16.4	1.6
B2	0.0852	2175	13.4	0.0753	0.0045	2182	5	16.4	1.5
B3	0.0776	2169	13.2	0.0698	0.0046	2177	5	16.3	1.6
C1	0.0660	2193	14.0	0.0604	0.0050	2198	6	16.7	2.0
C2	0.0512	2199	14.1	0.0484	0.0047	2204	8	17.4	2.7
C3	0.0373	2201	14.0	0.0378	0.0045	2208	11	18.6	3.8
OD	0.0410	2192	13.5	0.0387	0.0044	2200	10	17.4	3.5
OP	0.0314	2208	14.1	0.0330	0.0045	2215	11	19.1	4.0

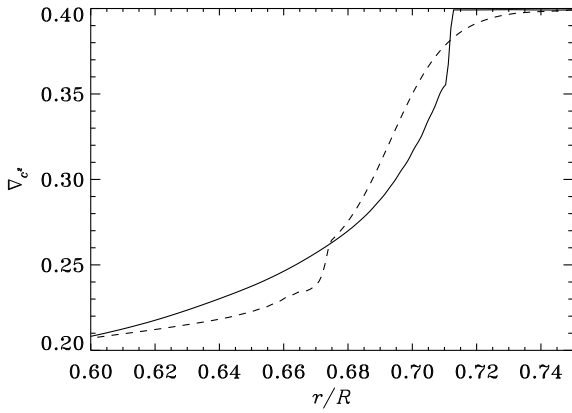


Figure 10. Gradients ∇_{c^2} of the squared sound speed in the reference Model S (solid line) and Model OP (dashed line), with a very smooth transition and a small opacity reduction near the base of the convection zone.

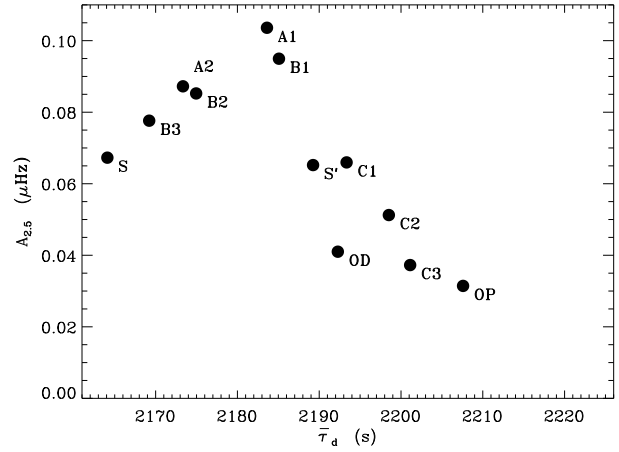


Figure 12. The symbols show the values of the amplitude $A_{2.5}$ versus acoustic depth $\bar{\tau}_d$ of the signal for all models listed in Table 2, obtained by fitting the noise-free frequencies (values listed in Table 3).

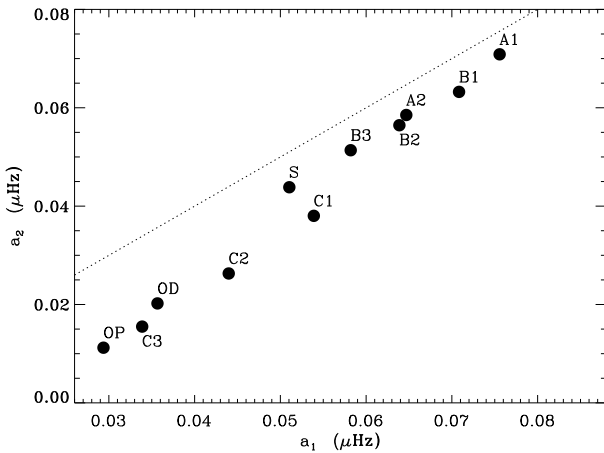


Figure 11. The stars show the values of the amplitude parameters a_1 and a_2 of the signal for all models listed in Table 3. The dotted line corresponds to $a_1 = a_2$.

in particular that, formally, a_2 arises from a discontinuity in the first derivative in the sound speed, while a_1 arises from a discontinuity in the second derivative. Thus one would expect a_2 to be bigger relative to a_1 for sharper transitions, as is indeed the case, although both terms contribute for all the cases considered. The corresponding inferred values of the amplitude $A_{2.5}$ for the models are shown in Fig. 12.

These results confirm what was already found by Christensen-Dalsgaard et al. (1995): in order to have an amplitude below what is found for the standard model S, a sub-adiabatic region within the proper convection zone (above the Schwarzschild boundary) is required.

5.2 Impact of noise on the seismic parameters

When noise is added, the inferred values of the parameters are affected. The values in the rightmost columns of Table 3 were obtained from fitting model data after adding solar noise. For each model, Monte Carlo simulations were run with 500 realizations of errors characteristic of a 72-d solar observational dataset.

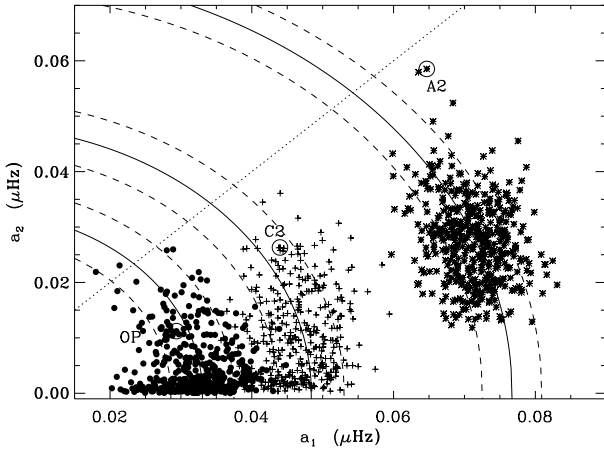


Figure 13. Examples for three models (A2 - stars; C2 - crosses; OP - filled circles) of the values a_2 and a_1 obtained from Monte Carlo simulations using solar uncertainties from a 72-d set of frequencies. The solid and dashed curves indicate the corresponding average combined amplitude $A_{2.5}$ (cf. Eq. 15) and the $\pm 1\sigma$ error interval on $A_{2.5}$. The values (a_1, a_2) obtained for the noise-free frequencies are also indicated as open circles for the three models (see Table 3).

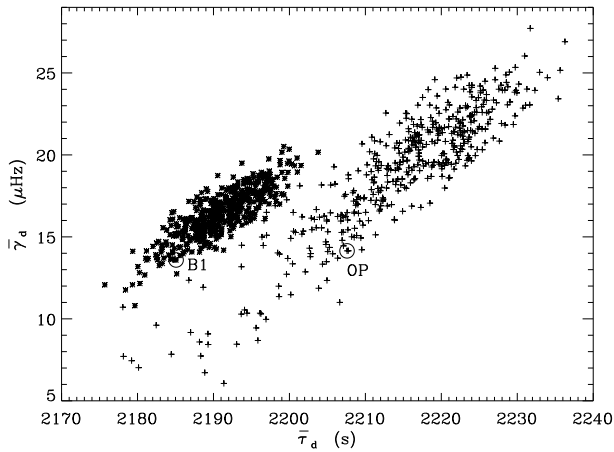


Figure 14. Values of $\bar{\tau}_d$ and $\bar{\gamma}_d$ for two models, B1 and OP, inferred from the Monte Carlo simulation, based on observed errors. Note the strong correlation between these two parameters, already shown for the solar data in Fig. 5. The open circles show the results of fitting the noise-free frequencies.

Figure 13 illustrates the effect on the individual amplitudes a_1 and a_2 for three models. It is clear from the figure that the added noise causes a systematic shift in the inferred values of a_1 and a_2 , with a_2 tending to be shifted to lower values, essentially corresponding to an apparently smoother transition. Similarly, although the value of $A_{2.5}$ is more robust, it suffers a reduction which, for the sharper transitions, may exceed 2σ : this is shown in Table 3 and is apparent for Model A2 in Fig. 13. Even so, the results confirm that, when properly calibrated for the presence of noise, the value of $A_{2.5}$ can be used to probe the sharpness of the base of the convection zone.

As is the case for solar data, the largest correlation between inferred parameters is that between $\bar{\tau}_d$ and $\bar{\gamma}_d$: the effect of noise on these two parameters for model data is shown in Fig. 14. The standard deviations of the inferred values of the parameters, and their

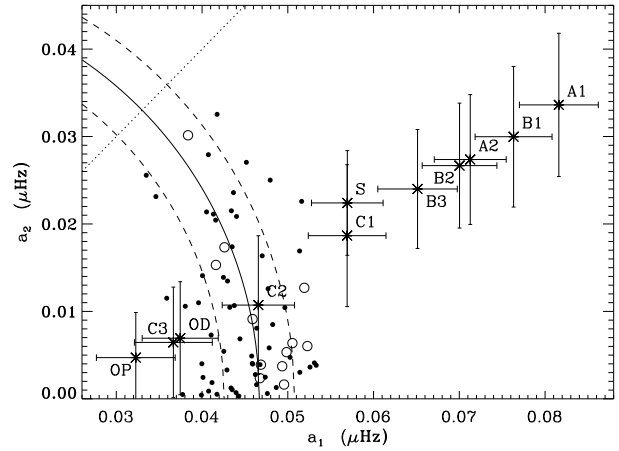


Figure 15. The stars show the average value from Monte Carlo simulations for the models using solar uncertainties, while the error bars are 1σ errors associated with those uncertainties, as given in Table 3. The dotted line corresponds to $a_1 = a_2$. The small filled circles show the fits to the individual observed 72-d datasets while the open circles are for 1 year datasets. The dashed lines show the $\pm 1\sigma$ range of $A_{2.5}$ around the mean value for the solar data (full line).

mean values, are listed in Table 3. In this table, the values found for the seismic parameters in the presence of observed uncertainties are listed in the last 6 columns, together with the 1σ uncertainties obtained through Monte Carlo simulations of 500 realizations. These use the uncertainties for a 72-d set of solar frequencies reported before.

As one would expect, the precision of the fitting is degraded when the amplitude is lower. In particular for $\bar{\tau}_d$ and $\bar{\gamma}_d$, as lower amplitude decreases the ability to separate the frequency and mode degree contributions for the argument of the signal, leading to a wider variation, within the correlation found, of these two parameters (see also Fig. 14).

We also note that, contrary to our previous work (Monteiro et al. 1994; Christensen-Dalsgaard et al. 1995), the option to estimate a priori the value of ϕ_0 and fix the value of Δ_d has resulted in an increase of the expected precision of the fitting for the three quantities listed in Table 1 (a_1 , a_2 , $\bar{\tau}_d$), required for testing the stratification of the overshoot layer. This improvement is crucial in securing a proper calibration of the key parameters associated with the sharpness and location of the base of the convection zone. The increase in precision comes at the expense of systematic shifts between the noise-free fits and the averages of the model fits including noise, as is evident in Table 3 as well as Figs 13 and 14. To correct for this the following comparison between the observations and the model results is based on the outcome of the Monte Carlo simulations for the latter.

6 RESULTS AND DISCUSSION

Based on the comparison of the fitting of the signal for the models (particularly in the presence of noise) and for the Sun, it is now possible to establish what are the implications for the stratification of the transition layer at the base of the convection zone.

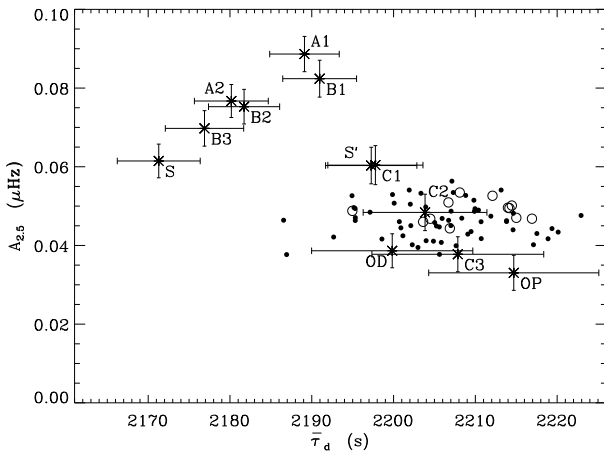


Figure 16. The small filled circles show the fits to the individual 72-d observed datasets while open circles are for 1 year datasets. The stars show the average values obtained for Monte Carlo simulations of the models with 1σ error bars, as listed in Table 3.

6.1 Comparing the models with the Sun

Figure 15 compares the amplitudes (a_1 and a_2) obtained from solar data with those obtained from model frequencies with solar-like noise added (cf. the noise-free case in Fig. 11). The model that seems most consistent with the solar observations, in this representation, is Model C2. This is confirmed by a comparison of the inferred values of $A_{2,5}$ and $\bar{\tau}_d$ for solar data and noisy model data (Fig. 16; cf. the noise-free case in Fig. 12). Model S and all the overshoot models in the A and B sequences exhibit amplitudes that are larger than what is inferred for the Sun. The models in the C sequence seem to span the range of solar amplitudes, with Model C2 providing the best fit. Model OP has a smaller amplitude than is inferred for the Sun, implying that the stratification in this model is even smoother than the average spherically symmetric radial stratification in the Sun.

It is more problematic to draw inferences from a comparison of model and solar values of the acoustic depth parameter $\bar{\tau}_d$, because the acoustic depth of the base of the convection zone is also strongly influenced by the sound-speed stratification in the rather uncertain near-surface layers. Specifically, the total acoustic size of the model and the acoustic location of the upper reflection boundary for each mode will have an impact on the value found for this parameter. Therefore its conversion into radial distance from the centre is not straightforward. We recall the values of $\bar{\tau}_d$ obtained for Models S and S', shown in Fig. 12, with a shift in the fitted values of $\bar{\tau}_d$ (error free data) of about 25 s. The only difference between these two models occurs at the surface, in order to bring the frequencies of S' much closer to the solar frequencies. Consequently this value is an indication on the accuracy we may expect on $\bar{\tau}_d$.

The fitting of the signal in the frequencies still suffers from some shortcomings, namely the incomplete representation of the dependence of the amplitude and argument of the signal on mode frequency and degree. On the other hand, the approach we have considered here uses a large number of modes (over 240), by including data up to mode degree of 20. Also we isolate the signal directly in the frequencies avoiding noise amplification that occurs when the signal is isolated in frequency differences. Both aspects are unique to our approach allowing in the case of the Sun a di-

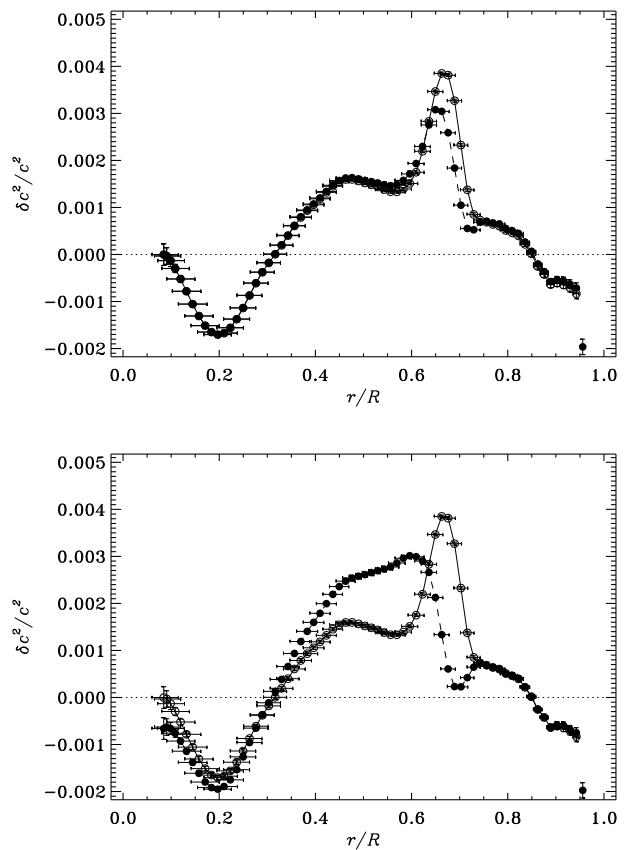


Figure 17. Relative differences $\delta c^2/c^2$, inferred by means of SOLA inversion, between the Sun and three solar models, in the sense (Sun) – (model). The analysis used the so-called ‘Best Set’ of observed frequencies of Basu et al. (1997). The vertical bars show the 1σ errors in the differences, estimated from the errors in the observed frequencies, while the horizontal bars provide a measure of the resolution of the inversion. In both panels the open symbols and solid line shows results for Model S. The closed symbols and dashed line are for Model A2 (upper panel) and Model C2 (lower panel).

rect and very precise study of the base of the solar convection zone. However, it is evidently also of great interest to investigate the extent to which information about the base of convective envelopes can be obtained from just low-degree data, as available in the foreseeable future from observations of other stars (see Monteiro et al. 2000).

In this investigation we are using seismic data to look at only one aspect of the solar structure, namely the sharpness and shape of the transition in stratification near the base of the convection zone. The seismic data contain much additional information about the solar interior, notably about the run of adiabatic sound speed with depth. The sound-speed differences between the Sun and three of the models considered here – Models S, A2 and C2 – inferred from helioseismic inversion of the data are illustrated in Fig. 17. The analysis was carried out using the so-called SOLA technique (see Rabello-Soares et al. 1999, for details on the implementation), following Christensen-Dalsgaard & Di Mauro (2007) and using the combined ‘Best Set’ of frequencies (Basu et al. 1997) extending to $l = 99$. Although there are statistically significant differences in sound speed between the Sun and Model S, these differences are small (0.4% in sound-speed squared, i.e. 0.2% in sound speed). The

differences between the illustrated models (A2 and C2) and the Sun are similarly small. In fact, although the models in this paper span a large range of behaviours in terms of the stratification near the base of the convection zone, we stress that they are all close to the Sun in terms of their small absolute differences in sound speed.

We remark that the details of the sound-speed gradient arising from overshoot in some cases may have substantial effects on the seismically inferred sound-speed differences between the Sun and the model. In Model C2, illustrated in the lower panel of Fig. 17 and in Fig. 6, the region where ∇_{c^2} is larger than in Model S leads to an increase in the sound speed just below the convection zone which largely eliminates the bump in δc^2 found with Model S. However, if this overshoot region were to be shifted to greater depth, thus eliminating the region of sub-adiabatic gradient in the lower part of the convection zone, the effect on the sound speed would be amplified to such an extent as to lead to a strong *negative* sound-speed difference between the Sun and the model. (To avoid this for the very smooth Model OP we had to invoke a small opacity reduction to shift the location of the boundary of the convection zone.) Thus it remains important to test the models both based on the properties of the signal associated with the acoustic glitch and based on the inferred sound-speed differences.

6.2 Implications for the stratification at the transition

As found by Christensen-Dalsgaard et al. (1995) standard models of the Sun either without or with the classical representation of overshoot, based on a non-local mixing-length formulation, are marginally inconsistent with the seismic data. In Fig. 16 both the amplitude for some models and for the solar data is shown. The reference Model S is outside the error bar of the data as well as any of the overshoot models calculated in the classical way. Even with a radiatively stratified overshoot layer the amplitude is found to be above the value found for the Sun. This is a clear indication that the transition at the base of the envelope requires a representation that is smooth over length scales of the order of the wavelength of the modes.

This clear preference is a strong indication in favour of stratifications that include a sub-adiabatic layer within the proper convection zone, as a necessary condition to obtain sufficiently smooth transitions that will be consistent with the solar data. Any model that includes overshoot will need to be extended from within the convection zone, replacing the commonly adopted procedure of adding an overshoot layer to the convective envelope as defined by the mixing-length theory (or equivalent).

The strong helioseismic preference for rather smooth profiles puts very strong constraints on many of the models we discussed in Sect. 1. In the following discussion we shall try to link the smoothness of the transition in the overshoot region to the underlying physical processes.

A common physical process relevant in most overshoot models is buoyancy braking, which decelerates downflow plumes once a positive temperature perturbation has been built up after travelling downward for a sufficient distance in a subadiabatic stratification. Buoyancy braking establishes a direct connection between the kinetic energy of downflows at the base of the convection zone and thermal properties of the overshoot region beneath. This leads to a relation between the Mach number M_a required at the base of the convection zone, the subadiabaticity as well as the depth of the overshoot region. Assuming for simplicity a constant value for the superadiabaticity $\delta = \nabla - \nabla_{\text{ad}}$, we can estimate temperature and

density perturbations as function of the overshoot depth, z , as follows:

$$\frac{T'}{T} \sim \frac{\rho'}{\rho} \sim \delta \frac{z}{H_p}. \quad (17)$$

Buoyancy braking gives a relation between the kinetic energy of the plume at the base of the convection zone and the buoyancy work in the overshoot region:

$$\frac{1}{2}\rho v^2 \sim \frac{1}{2}g\rho'z = \frac{1}{2}\rho\delta g H_p \left(\frac{z}{H_p}\right)^2, \quad (18)$$

where g is the gravitational acceleration. Combining both equations leads to (neglecting factors of order unity):

$$M_a^2 \sim \delta \left(\frac{z}{H_p}\right)^2. \quad (19)$$

In the traditional non-local mixing-length overshoot models we have $z \simeq 0.2H_p$ and $\delta \simeq 10^{-6}$ leading to $M_a \simeq 2 \times 10^{-4}$, which corresponds to a convective velocity of about 40 m s^{-1} , consistent with mixing-length models assuming a filling factor of about 0.1. Having a smooth transition of the overshoot from nearly adiabatic to radiative temperature gradients requires that the average values for δ are of the order of 0.05. In that case our estimate requires $M_a \simeq 0.05$ corresponding to a convective velocity of about 10 km s^{-1} at the base of the convection zone. The latter is (if at all) only possible if the filling factor for downflow plumes is very small. This is an inevitable consequence of buoyancy braking, which applies to overshoot models in a very general sense, whether numerical 3D simulation or any other simplified treatment. The key for the argumentation above is the fact that a smooth overshoot profile implies automatically substantial deviations from adiabaticity in an extended region that is convectively mixed. Many of the numerical overshoot simulations to date show smooth transitions. However, the latter are to a large degree related to numerical setups that have either a reduced stiffness in the radiative interior or have large energy fluxes (to reduce thermal relaxation time scales) that result in much larger Mach numbers and allow consequently for smooth overshoot profiles with substantial deviations from adiabaticity. Käpylä et al. (2007) presented a series of numerical experiments that show the return to more adiabatic step-like overshoot profiles with reduction of the overall energy flux. Extrapolating these results to the solar energy flux seems to make a step-like quasi-adiabatic overshoot almost inevitable. The investigation of Rempel (2004) aimed at understanding the physical parameters under which a smooth transition can be expected. The two necessary conditions found were that a) the downflow filling factor is small and b) there is a continuous distribution of downflow strength. While the latter is a natural consequence of convection, the former is very controversial and not supported by any numerical simulations we know about (the required downflow filling factors would be smaller than 10^{-4}).

Overall it appears that within the framework of models discussed above it is almost impossible to obtain sufficiently smooth profiles that agree with the helioseismic constraints. This difficulty is strongly related to the effective role of buoyancy braking in the overshoot region. Only if we relax this assumption is it possible to obtain smooth overshoot profiles for moderate Mach numbers. It has been suggested by Petrovay & Marik (1995) that smooth overshoot profiles can be easily obtained once the assumption of a strong correlation between vertical velocity and temperature fluctuation is dropped. They suggested that in the extreme case of vanishing correlation the penetration is only limited by turbulent dissipation, with no impact on the thermal stratification. For a smoothly

diminishing correlation a smooth transition of all overshoot quantities results.

Xiong & Deng (2001), in fact, presented a model that leads to such very smooth transitions, by using a non-local convection model that is based on a moment approach computing auto and cross-correlations of turbulent velocity and temperature (Xiong 1989). This model predicts a strong decorrelation of velocity and temperature fluctuation in the lower overshoot region of the Sun, while the authors find a strong anticorrelation in the upper overshoot region above the photosphere. The difference between the overshoot regions is attributed to the values of the Péclet number, which are much smaller than unity in the photosphere and much larger in overshoot region at the base of the convection zone. The overall outcome is a temperature profile that is very similar to the best match we found in this investigation. Their overshoot region extends about $0.6H_p$ beneath the convection zone and shows already a significantly subadiabatic stratification within the lower parts of the convection zone. Recently Marik & Petrovay (2002) used a different non-local model based on the formulation of Canuto & Dubovikov (1997) and Canuto & Dubovikov (1998) and found overshoot of only $0.06H_p$. While still much smoother than the sharp profiles of non-local mixing-length theory, this model provided again a temperature profile that stayed closed to adiabatic for significant extent of the overshoot depth. This class of models involves a number of assumptions, including the treatment of closure, and parameters generally determined from laboratory experiments or atmospheric or oceanographic measurements; thus a thorough study of their applicability under stellar conditions is indicated. In addition, a further investigation is required of the differences between the Xiong & Deng (2001) and the Canuto & Dubovikov (1997) approaches.

Another possibility could be a spatial or temporal inhomogeneity of overshoot leading to an average profile looking more smooth; however as estimated below this possibility seems unreasonable, too:

Assume that we have a large filling factor ~ 0.1 so that the overshoot profile has a very sharp transition. Intermittent downflows are able to perturb the sharp boundary between the almost adiabatic overshoot and the underlying strongly subadiabatic radiative zone. The consequence are buoyancy oscillations with the Brunt Väisälä frequency $\omega_{BV} = \sqrt{g|\delta|/H_p}$. Due to the sharp transition toward the radiation zone, ω_{BV} would be given by the radiative values just beneath the overshoot region. With a value of $d\nabla_{\text{rad}}/dr = 10^{-8} \text{ m}^{-1}$ at the base of the convection zone, overshoot with a depth d_{os} leads to a value of $\delta = -(d\nabla_{\text{rad}}/dr)d_{os}$. Using $d_{os} = 0.1 H_p$, $g = 500 \text{ m s}^{-2}$, $H_p = 60 \text{ Mm}$ yields $\omega_{BV} \sim 7 \times 10^{-4} \text{ s}^{-1}$. Amplitude d and velocity v of the buoyancy oscillations at the overshoot radiative interior interface are related by $v = \omega_{BV}d$, where v should be of the order of the convective motions perturbing the interface. Using a value of $v = 100 \text{ m s}^{-1}$ yields $d = 140 \text{ km}$, which is comparable to the thickness of the transition expected from the overshoot model in the first place. A larger amplitude requires a larger v , which can be only obtained by having faster downflows, meaning smaller filling factor (so nothing is gained here). We note that the above discussion implicitly assumed again a strong correlation between temperature and velocity fluctuations.

It has been also speculated that the depth of overshoot depends on latitude, due to the changing influence of rotation on convective motions. The study of Brummell et al. (2002) found the deepest penetration at pole and equator and a minimum at around 30° latitude with about 60% of the maximum overshoot depth. This result was obtained by placing small Cartesian simulation domains (with

periodic boundaries in the horizontal direction) at different latitude positions. Having a variation of overshoot depth in a global model adds additional complexity to the problem, since regions with different vertical temperature structures have to be in horizontal force balance. These temperature differences can be estimated from Eq. (17) and can be quite substantial. Restricting T' to 100 K allows with $\delta \sim 0.1$, $T \sim 2 \times 10^6 \text{ K}$ and $H_p = 50 \text{ Mm}$ for only a displacement of 25 km. A global force balance in latitude would require either zonal flows or magnetic forces of substantial strength – at least the zonal flows should leave observable helioseismic signatures given the fact that only about 10 K temperature difference are required in the convection zone to balance the deviations of differential rotation from the Taylor-Proudman state. Without these flows or magnetic field such a configuration cannot be in a hydrostatic balance and would return to spherical symmetry on a time scale given by ω_{BV} .

7 CONCLUSIONS

We have considered a variety of models with different stratification near the base of the convection zone, using a parameterization of the stratification that is motivated by models that have a spectrum of overshooting plumes with a range of depths of penetration. From the range of models we have considered, we find that a relatively smooth model (Model C2) fits the helioseismic data better than a standard model without convective overshoot, and better also than simple convective overshoot models which possess a more-or-less sharp transition to subadiabatic stratification beneath an overshoot region which is a nearly adiabatic extension of the convection zone. Thus a model characterized by an overshoot layer extending for $\ell_{ov}/H_p \approx 0.37$ is compatible with the solar data, corresponding to an additional fully mixed zone of about 3% in radius. Of course it is desirable that solar models be built whose stratification is determined self-consistently from the physics underlying the model, but the parameterization used here may be a reasonable way of approximating such stratification in the context of simple spherically symmetric models.

Our investigation method is very similar to that developed by Monteiro et al. (1994), though with some differences due to the fact that here we determine the phase ϕ_0 independent of our fitting to the oscillatory signal in the frequencies, and therefore we fit amplitude parameters a_1 and a_2 separately. It should though be noted that we find that the fitted values of a_1 and a_2 are not independent, probably because the frequency range of the modes used in the fitting is rather small and insufficient fully to separate the frequency dependent terms of the amplitude, and so their separate values cannot be relied upon. Indeed we find that noise in model data tends to cause the value of a_2 to be significantly underestimated, relative to its fitted value for noise-free data. We find, however, that the combination amplitude $A_{2,5}$ is a more robust indication of the sharpness of the transition in stratification near the convection-zone base.

Our selection of models demonstrates that the signal analysis here is sensitive to acoustic glitches that would barely be noticed through helioseismic inversion which provides averages over such features. On the other hand, our analysis is by design insensitive to smooth differences between the Sun and the model, including very substantial differences in the sound speed which would be obvious from an inverse analysis. Thus these two techniques are obviously complementary in their ability to characterize the properties of the solar interior.

It may be remarked that we have used models similar

to Model S, which incorporates the “old” solar element abundances of Grevesse & Noels (1993), rather than the “new” abundances suggested by the work of Asplund and collaborators (e.g., Asplund et al. 2009). The new abundances are known to modify the opacities in the solar interior in such a way as to produce models that are strongly in disagreement with the stratification inferred from helioseismology in the radiative interior, the largest discrepancy being in the vicinity of the base of the convection zone. Since our aim in this work is to investigate the subtle effects of overshoot in this region, it is prudent to start with models that are broadly consistent with the known stratification of the Sun’s interior, rather than models based on the newer abundances that are further away from the Sun’s stratification.

Although the present analysis makes use of the full range of modes that are sensitive to the base of the convection zone, similar analyses are possible given just the low-degree modes available in observations of distant stars in the foreseeable future (e.g., Monteiro et al. 2000; Ballot et al. 2004; Piau et al. 2005). This is potentially an important complement to the more detailed solar data, particularly given the very long timeseries and hence high frequency precision that will be obtained with the *Kepler* mission (e.g., Gilliland et al. 2010) as well as from planned dedicated ground-based facilities.

From this investigation we can conclude that i) overshoot is necessary to improve the agreement between models and helioseismic constraints, ii) the required overshoot profiles are outside the realm of the classic “ballistic” overshoot models and iii) the lower part of the convection zone is likely substantially subadiabatic. We cannot measure the latter directly, but our investigation indicates that the required level of smoothness cannot be achieved without iii). Currently only non-local convection models that are based on auto- and cross-correlations of velocity and temperature perturbations are capable of providing overshoot profiles with the desired degree of smoothness in the transition. However, these theories have hidden parameters and rely on closure models. To our current knowledge there has not yet been a thorough study on how robust the properties of overshoot (under the conditions found at the base of the solar convection zone) are within the framework of these models. We hope that our investigation motivates more research in that direction. The indication that the lower part of the convection zone could be substantially subadiabatic (with values of $|\nabla - \nabla_{\text{ad}}| > 10^{-3}$) has profound consequences for the storage and stability of magnetic field and the overall role that the lower convection zone (not just the overshoot region) might play in the solar magnetic cycle.

ACKNOWLEDGMENTS

We thank the referee for constructive and helpful comments on an earlier version of the manuscript, which have improved the presentation. MJM was supported in part through project PTDC/CTE-AST/098754/2008, funded by FCT/MCTES Portugal and by the European programme FEDER. This work was supported by the European Helio- and Asteroseismology Network (HELAS), a major international collaboration funded by the European Commission’s Sixth Framework Programme.

REFERENCES

- Asplund M., Grevesse N., Sauval A. J., Scott P., 2009, *ARAA*, 47, 481
- Bahcall J. N., Pinsonneault M. H., 1995, *Rev. Mod. Phys.*, 67, 781
- Ballot J., Turck-Chièze S., García R. A., 2004, *A&A*, 423, 1051
- Ballot J., Jiménez-Reyes S. J., García R. A., 2006, in Fletcher K., ed., *Proc. SOHO 18 / GONG 2006 / HELAS I Conference*, Beyond the spherical Sun. ESA Publications Division, Noordwijk, ESA Special Publications, 624, P56
- Basu S., Antia H. M., 1994, *MNRAS*, 269, 1137
- , 2001, *MNRAS*, 324, 498
- Basu S., Mandal A., 2004, *ApJ*, 617, L155
- Basu S., Antia H. M., Narasimha D., 1994, *MNRAS*, 267, 209
- Basu S., Chaplin W. J., Christensen-Dalsgaard J., Elsworth Y., Isaak G. R., New R., Schou J., Thompson M. J., Tomczyk S., 1997, *MNRAS*, 292, 243
- Baturin V. A., Mironova I. V., 2010, *ApSS*, 328, 265
- Brummell N. H., Clune T. L., Toomre J., 2002, *ApJ*, 570, 825
- Canuto V. M., Dubovikov M., 1997, *ApJ*, 484, 161
- , 1998, *ApJ*, 493, 834
- Christensen-Dalsgaard J., 2008a, *ApSS*, 316, 13
- , 2008b, *ApSS*, 316, 113
- Christensen-Dalsgaard J., Di Mauro M. P., 2007, in Straka C. W., Lebreton Y., Monteiro M. J. P. F. G., eds, *Stellar Evolution and Seismic Tools for Asteroseismology: Diffusive Processes in Stars and Seismic Analysis*, EAS Publ. Ser., 26, EDP Sciences, Les Ulis, France, p. 3
- Christensen-Dalsgaard J., Pérez Hernández F., 1992, *MNRAS*, 257, 62
- Christensen-Dalsgaard J., Gough D. O., Pérez Hernández F., 1988, *MNRAS*, 235, 875
- Christensen-Dalsgaard J., Gough D. O., Thompson M. J., 1989, *MNRAS*, 238, 481
- Christensen-Dalsgaard J., Monteiro M. J. P. F. G., Thompson M. J., 1995, *MNRAS*, 276, 283
- Christensen-Dalsgaard J., Däppen W., Ajukov S. V., et al., 1996, *Science*, 272, 1286
- Deng L., Xiong D. R., 2008, *MNRAS*, 386, 1979
- Duvall T. L., 1982, *Nature*, 300, 242
- Gilliland R. L., Brown T. M., Christensen-Dalsgaard J., et al., 2010, *PASP*, 122, 131
- Gough D. O., 1990, in Osaki Y., Shibahashi H., eds, *Progress of seismology of the sun and stars*, *Lecture Notes in Physics*, vol. 367, Springer, Berlin, p. 283
- Gough D. O., 1995, in Hoeksema J. T., Domingo V., Fleck B., Battrick B., eds, *Proc. Fourth SOHO Workshop, Helioseismology*. ESA Publications Division, ESA Special Publications, 376 (1), 181
- Gough D. O., 2002a, in Favata F., Roxburgh I. W., Galadí-Enríquez D., eds, *Proc. 1st Eddington Workshop, Stellar Structure and Habitable Planet Finding*. ESA Publications Division, ESA Special Publications, 485, 65
- Gough D. O., 2002b, in *Proc. SOHO 11 Symposium, From solar Min to Max: half a solar cycle with SOHO*. ESA Publications Division, ESA Special Publications, 508, 577
- Grevesse N., Noels A., 1993, in Prantzos N., Vangioni-Flam E., Cassé M., eds, *Origin and Evolution of the Elements*. Cambridge Univ. Press, 15
- Houdek G., Gough D. O., 2007, *MNRAS*, 375, 861
- Hurlburt N. E., Toomre J., Massaguer J. M., Zahn J., 1994, *ApJ*, 421, 245

- Iglesias C. A., Rogers F. J., Wilson B. G., 1992, *ApJ*, 397, 717
- Käpylä P. J., Korpi M. J., Stix M., Tuominen I., 2007, in Kupka F., Roxburgh I. W., Chan K. L., eds, *Proc. IAU Symposium 239, Convection in Astrophysics*. International Astronomical Union and Cambridge University Press, p. 437
- Libbrecht K. G., Woodard M. F., 1990, *Nature*, 345, 779
- Marik M., Petrovay K., 2002, *A&A*, 396, 1011
- Michaud G., Proffitt C. R., 1993, in Baglin A., Weiss W. W., eds, *Proc. IAU Colloq. 137, Inside the stars*. Astronomical Society of the Pacific, San Francisco, ASP Conf. Ser., 40, p. 246
- Monteiro M. J. P. F. G., Thompson M. J., 1998, in Korzennik S. G., Wilson A., eds, *Structure and Dynamics of the Interior of the Sun and Sun-like Stars*. ESA Publications Division, ESA Special Publications, 418, 819
- , 2005, *MNRAS*, 361, 1187
- Monteiro M. J. P. F. G., Christensen-Dalsgaard J., Thompson M. J., 1994, *A&A*, 283, 247
- , 2000, *MNRAS*, 316, 165
- , 2002, in Favata F., Roxburgh I. W., Galadí-Enríquez D., eds, *Proc. 1st Eddington Workshop, Stellar Structure and Habitable Planet Finding*. ESA Publications Division, ESA Special Publications, 485, 291
- Petrovay, K., Marik, M., 1995, in Ulrich R. K., Rhodes E. J., Däppen W., eds, *Proc. GONG'94: Helio- and Asteroseismology from Earth and Space*. Astronomical Society of the Pacific, San Francisco, ASP Conf. Ser., 76, p. 216
- Piau L., Ballot J., Turck-Chièze S., 2005, *A&A*, 430, 571
- Rabello-Soares M. C., Basu S., Christensen-Dalsgaard J., 1999, *MNRAS*, 309, 35
- Rempel M., 2004, *ApJ*, 607, 1046
- Rogers F. J., Swenson F. J., Iglesias C. A., 1996, *ApJ*, 456, 902
- Rogers T. M., Glatzmaier G. A., 2005a, *MNRAS*, 364, 1135
- , 2005b, *ApJ*, 620, 432
- Roxburgh I. W., Simmons J., 1993, *A&A*, 277, 93
- Roxburgh I. W., Vorontsov S. V., 1994, *MNRAS*, 268, 880
- , 1996, *MNRAS*, 278, 940
- Saikia E., Singh H. P., Chan K. L., Roxburgh I. W., Srivastava M. P., 2000, *ApJ*, 529, 402
- Schmitt J. H. M. M., Rosner R., Bohn H. U., 1984, *ApJ*, 282, 316
- Schou J., 1999, *ApJ*, 523, L181
- Singh H. P., Roxburgh I. W., Chan K. L., 1995, *A&A*, 295, 703
- , 1998, *A&A*, 340, 178
- van Ballegooijen A. A., 1982, *A&A*, 106, 43
- Verner G. A., Chaplin W. J., Elsworth Y., 2006, *ApJ*, 638, 440
- Vorontsov S. V., Baturin V. A., Pamyatnykh A. A., 1991, *Nature*, 349, 49
- Xiong D. R., 1989, *A&A*, 209, 126
- Xiong D. R., Deng L., 2001, *MNRAS*, 327, 1137
- Zahn J.-P., 1991, *A&A*, 252, 179

APPENDIX A: DETERMINING THE PHASE OF SOLAR EIGENFUNCTIONS

A1 The eigenfunction phase

The phase $\phi(\omega, l)$ in Eq. (9) is obviously closely related to the eigenfunctions of the oscillations and hence can be determined from fits to those eigenfunctions. This was discussed in detail by Christensen-Dalsgaard & Pérez Hernández (1992) (see also Roxburgh & Vorontsov 1996), in the context of the Duvall (1982) law. According to this, the frequencies satisfy

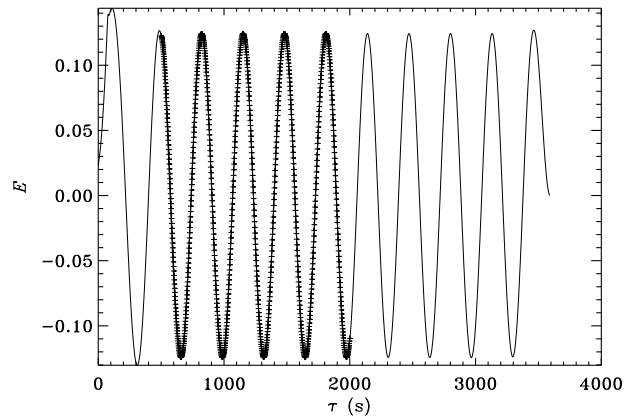


Figure A1. Scaled eigenfunction $E = (\rho c)^{1/2} r \xi_r$, for the mode with $l = 0$, $n = 21$ in Model S, as a function of acoustic depth τ . The crosses show the results of fitting the asymptotic eigenfunction.

$$\int_{r_1}^R \left(1 - \frac{L^2 c^2}{\omega^2 r^2}\right)^{1/2} \frac{dr}{c} = \frac{\pi[n + \alpha(\omega, l)]}{\omega}, \quad (\text{A1})$$

where $L^2 = l(l + 1)$. This is obtained from Eq. (8) by applying the appropriate inner boundary conditions, with ϕ and α being related by

$$\phi = -\left(\alpha + \frac{1}{4}\right)\pi. \quad (\text{A2})$$

For simplicity we neglect the higher-order terms in the near-surface behaviour and assume that α , and hence ϕ , are functions of ω alone. The quantity ϕ_0 entering into the fitting formula is the intercept at $\omega = 0$ in a linear fit to ϕ as a function of ω and hence can be determined from a similar fit to α .

Christensen-Dalsgaard & Pérez Hernández (1992) analysed the dependence of α on the properties of solar models by fitting Eqs (8) and (9) to computed solutions of the equations of radial oscillations in the models, assuming only the surface boundary conditions and hence determining α as a continuous function of ω (a similar procedure has been used by Roxburgh & Vorontsov 1996). Here we consider instead full eigenfunctions of the model, over a range of degrees, to approximate more closely the actual fits. As a simplification, we use only relatively low-degree modes and apply the fit rather close to the stellar surface. Then Eqs (8) and (9) can be approximated by

$$\xi_r = A(\rho c)^{-1/2} r^{-1} \cos(\omega\tau + \phi), \quad (\text{A3})$$

in terms of the acoustic depth τ (cf. Eq. 3). We therefore fit $A \cos(\omega\tau + \phi)$ to $E = (\rho c)^{1/2} r \xi_r$ in a least-squares sense, over a suitable interval $[\tau_1, \tau_2]$ in τ .

As an example we consider Model S (Christensen-Dalsgaard et al. 1996). Figure A1 shows an example of the fit to an eigenfunction, for the mode with $l = 0$, $n = 21$. The fit was made in the interval between 500 s and 2000 s in τ . As illustrated by the crosses, the fit is excellent.

To determine $\phi(\omega)$ we consider modes in the interval $5 \leq l \leq 10$; also, in accordance with the mode sets used in the fit for the base of the convection zone, we consider frequencies between 1.9 and 4 mHz. The phases resulting from the fit are shown in Fig. A2, confirming that the scatter at given frequency is modest. Also shown is a least-squares fit of a straight line which yields $\phi_0 = 0.890$, and a

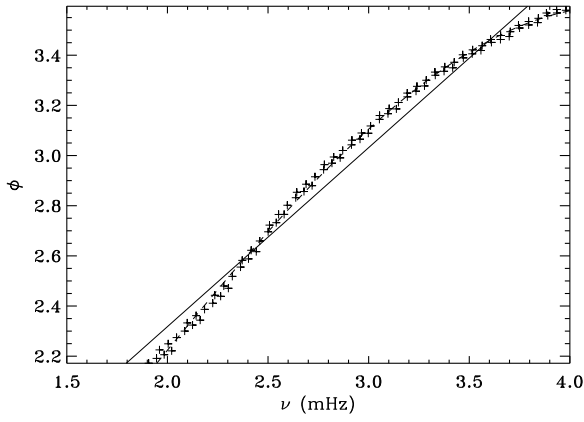


Figure A2. Fitted phases for modes between 5 and 10 in degree and 1.9 and 4 mHz in cyclic frequency $\nu = \omega/2\pi$, in Model S. The solid and (barely visible) dashed curves show linear and cubic least-squares fits to the points, respectively.

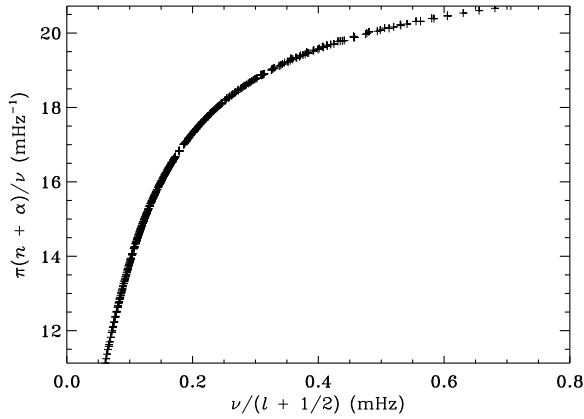


Figure A3. Duvall plot for the modes between 5 and 100 in degree and 1.9 and 4 mHz in frequency, in Model S, determining α from the cubic fit to the phase in Fig. A2.

cubic fit which follows the computed points very closely but yields an intercept at $\omega = 0$ of 0.503.

The Duvall relation resulting from ϕ , and hence α , determined in this manner is illustrated in Fig. A3, using $\alpha(\omega)$ as obtained from the cubic fit in Fig. A2. Here all modes with $5 \leq l \leq 100$ and frequency between 1.9 and 4 mHz are included. The match to the Duvall law is very good, strongly indicating that ϕ as determined from the low-degree modes can be applied over a broad range of degrees.

A2 Differential phase determination

While the eigenfunction fit provides the most appropriate phase $\phi(\omega)$ for the models, and hence presumably an appropriate estimate of ϕ_0 , this is obviously not possible for the observations. However, the results above suggest that an estimate of ϕ and ϕ_0 can be obtained from a fit of the Duvall relation. One possibility would be to determine the function $\alpha(\omega)$ that most successfully collapses the points in the Duvall plot to a curve and to obtain $\phi(\omega)$ from that.

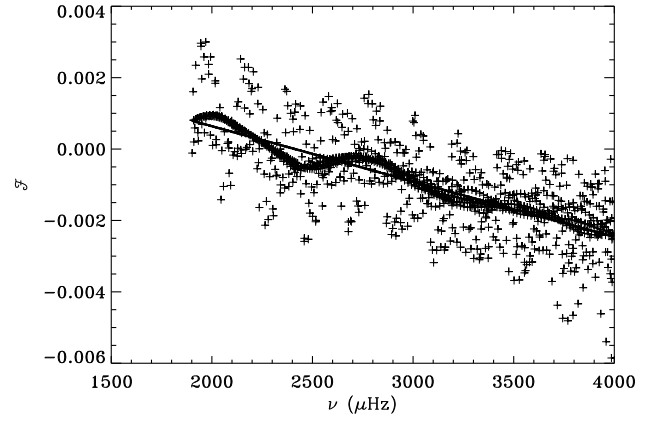


Figure A4. The predominantly frequency-dependent residual difference \mathcal{F} (cf. Eq. A9) resulting from a fit to frequency differences between Model C2 and Model S, using Eq. (A8). The straight line shows a linear least-squares fit to the results, resulting in a determination of ϕ_0 .

A possibly simpler approach is to use the differential form of the Duvall law (Christensen-Dalsgaard et al. 1988) to determine a correction to ϕ_0 , relative to a suitable reference model. By linearizing Eq. (A1) in small changes δc and $\delta \alpha$ we obtain

$$S \frac{\delta \omega}{\omega} = \mathcal{H}_1(\omega/L) + \mathcal{H}_2(\omega), \quad (\text{A4})$$

where

$$S = \int_{r_1}^R \left(1 - \frac{L^2 c^2}{\omega^2 r^2}\right)^{-1/2} \frac{dr}{c} - \pi \frac{d\alpha}{d\omega}, \quad (\text{A5})$$

$$\mathcal{H}_1(\omega) = \int_{r_1}^R \left(1 - \frac{c^2}{\omega^2 r^2}\right)^{-1/2} \frac{dr}{c}, \quad (\text{A6})$$

and

$$\mathcal{H}_2(\omega) = \frac{\pi}{\omega} \delta \alpha(\omega). \quad (\text{A7})$$

As discussed by Christensen-Dalsgaard et al. (1989) the functions \mathcal{H}_1 and \mathcal{H}_2 can be approximated by a double-spline fit to the scaled frequency differences, to obtain $\tilde{\mathcal{H}}_1$ and $\tilde{\mathcal{H}}_2$. Given $\tilde{\mathcal{H}}_2$, Eqs (A2) and (A7) show that the difference in the phase can be obtained as

$$\delta \phi = -\pi \delta \alpha \approx -\omega \tilde{\mathcal{H}}_2. \quad (\text{A8})$$

It should be noticed that a fit of the form given in Eq. (A4) can only determine the functions \mathcal{H}_1 and \mathcal{H}_2 to within a constant. Consequently, $\delta \phi$ as determined from Eq. (A8) is only determined to within a constant multiple of ω . Obviously, this has no effect on the inferred value of $\delta \phi_0$.

We have tested this procedure by applying it to a few of the models discussed in Section 5.1. Here the frequency range was, as usual, between 1.9 and 4 mHz, and modes of degree between 0 and 100 were included. For simplicity, the term in $d\alpha/d\omega$ was neglected in computing S from Eq. (A5). To determine $\delta \phi_0$ we carry out the fit to determine the function $\tilde{\mathcal{H}}_1(\omega/L)$ and evaluate

$$\mathcal{F} = -(S \delta \omega - \omega \tilde{\mathcal{H}}_1); \quad (\text{A9})$$

we then carry out a linear least-squares fit to \mathcal{F} , as a function of frequency, resulting in $\delta \phi_0$. The procedure is illustrated in Fig. A4, for Model C2. In Table A1, the result is compared with the actual difference in ϕ_0 , relative to Model S, obtained by fitting the eigen-

Table A1. Phases and phase differences resulting from eigenfunction and differential Duvall fits; $\delta\phi_0^{(1)}$ is the difference relative to Model S computed directly from ϕ_0 for the two models, while $\delta\phi_0^{(2)}$ is the corresponding difference inferred from the differential asymptotic Duvall fit (Eq. A8). The solar result of the differential asymptotic analysis used a 72-d MDI dataset starting in April 1996.

Type	ID	ϕ_0	$\delta\phi_0^{(1)}$	$\delta\phi_0^{(2)}$
Model				
	S	0.8904	–	–
	C2	0.8944	0.0040	0.0037
	OP	0.8954	0.0050	0.0047
	S'	0.5485	-0.3419	-0.3257
Sun				
		–	–	-0.3181

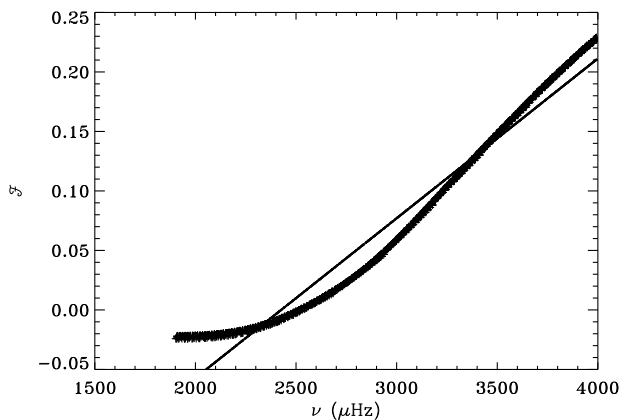


Figure A5. The predominantly frequency-dependent residual difference \mathcal{F} resulting from a fit to frequency differences between Model S' and Model S, using Eq. (A8). See caption to Fig. A4.

functions in the two models; the agreement is clearly quite good. Table A1 also lists the very similar results for Model OP.

As a more extreme example, we consider a model, Model S', based on Model S but modified to suppress the dominant, near-surface part of the differences between the observed frequencies and those of Model S (e.g., Christensen-Dalsgaard et al. 1996). Specifically, Γ_1 was modified by multiplying it by

$$1 - 0.4 \exp\left[\frac{(r-r_0)^2}{\Delta r^2}\right], \quad (\text{A10})$$

where $r_0 = (1 - 2.5 \times 10^{-4})R$ and $\Delta r = 1.5 \times 10^{-4}R$. This was designed to emulate the effect of turbulent pressure on the thermodynamics of the strongly superadiabatic part of the convection zone (C. S. Rosenthal, private communication). The differences between the frequencies of this model and those of Model S essentially match the corresponding differences for the observed frequencies and hence contain a large frequency-dependent component (after scaling). This is reflected in the large frequency-dependent part of the frequency differences and hence in the resulting \mathcal{F} , illustrated in Fig. A5. The value of $\delta\phi_0$ obtained from fitting to \mathcal{F} is listed in Table A1, together with the value resulting from the fits to the eigenfunctions. Remarkably, even for this very substantial difference there is reasonable agreement with the directly determined values of ϕ_0 for the models, indicating that the differential Duvall

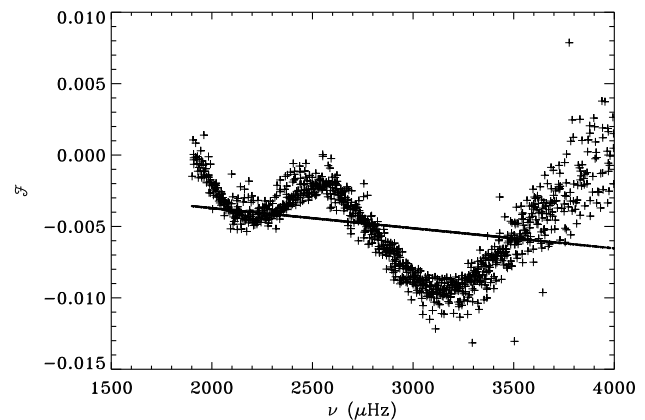


Figure A6. The predominantly frequency-dependent residual difference \mathcal{F} (cf. Eq. A9) resulting from a fit to frequency differences between MDI observations and Model S', using Eq. (A8). The observations were the 72-d set used in Table A1. See caption to Fig. A4.

analysis provides a robust method for estimating ϕ_0 , also for observed frequencies.

We have also applied the differential Duvall analysis to a 72-d set of MDI observed frequencies. As shown in Table A1 this yields a $\delta\phi_0$ very similar to that obtained for Model S'; this was to be expected, given that this model was fitted to the observed frequencies.

In the fits of model frequencies to Eq. (11) we used the value of ϕ_0 resulting from a fit to the corresponding eigenfunctions. In the analysis of the observed frequencies, we have used Model S' as a reference; in this way we hope to minimize any systematic effects that would result from the larger frequency differences relative to Model S. As an example, Fig. A6 shows the phase-difference plot for one of the 72-d observational sets. The linear fit gives $\delta\phi_0 = -8.9 \times 10^{-4}$, again indicating that Model S' provides a good fit to the observations. It is likely that the oscillatory component arises from a combination of the residual effects of the acoustic glitch associated with the second helium ionization zone (e.g., Gough 1990; Vorontsov et al. 1991; Monteiro & Thompson 2005) and a component of the near-surface difference which has not been eliminated by the modification (A10) to Γ_1 . The former effect would indicate that the helium abundance (or the equation of state) in the model (and hence in Model S) is not in full agreement with that of the Sun; taken at face value the variation below 2500 μHz suggests that the envelope helium abundance of 0.245 in the model is too low by about 0.008.

A3 Solar-cycle variation

We have carried out the differential fit to determine the value of $\delta\phi_0$ and hence ϕ_0 for all the datasets involved in the analysis. The results for the 72-d sets were illustrated in Fig. 2 which clearly reflects the variation in solar activity. To understand the behaviour of the variation we compare observed frequencies at an arbitrary phase of the solar cycle with frequencies at solar minimum and recall that the frequencies increase with solar activity, the change being a steeply increasing function of frequency (e.g., Libbrecht & Woodard 1990). We also note that \mathcal{H}_2 essentially corresponds to the scaled relative frequency differences, apart from the arbitrary constant in the separation into \mathcal{H}_1 and \mathcal{H}_2 in Eq. (A4). Thus \mathcal{H}_2 increases with increasing frequency. Choosing the con-

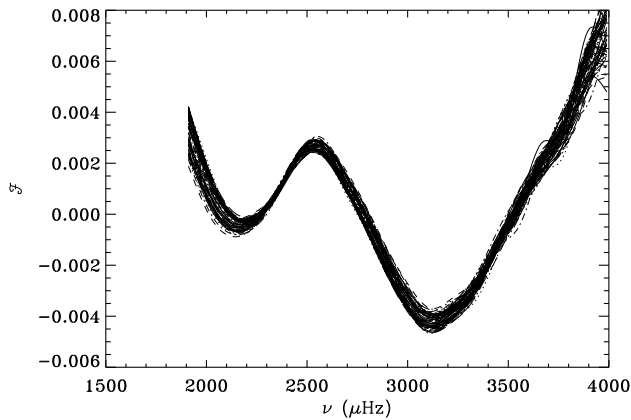


Figure A7. The functions $-\omega\mathcal{H}_2$ resulting from the spline fit (cf. Eq. A4) to the frequency differences between all sets of 72-d observations and Model S' , after subtraction of the linear fits to the corresponding \mathcal{F} .

stant such that \mathcal{H}_2 is zero at the low end of the frequency range considered, the function \mathcal{F} is similarly zero at low frequency but with a negative slope. Consequently, the intercept $\delta\phi_0$ at zero frequency, which is obviously unaffected by the choice of constant, is positive, as observed in Fig. 2, and increases with increasing solar activity and hence increasing frequency.

There have been suggestions that the effect of the glitch associated with the second helium ionization zone varies with the phase of the solar cycle (Gough 1995, 2002b; Basu & Mandel 2004; Ballot et al. 2006; Verner et al. 2006). We would expect that such a variation should be visible also in \mathcal{F} . To investigate this, Fig. A7 combines the fitted \mathcal{H}_2 for all 72-d observations, after subtraction of the linear fit. There is evidently very little scatter in the result, and further inspection shows no evidence for systematic variations with the phase of the solar cycle. Similarly, the second differences in the smooth component of the frequencies (see the lower panel of Fig. 3) show no significant variation with solar cycle. To set the scale, we note that the change $\delta\nu$ in cyclic frequency, corresponding to a change $\delta\mathcal{F}$ in \mathcal{F} , approximately satisfies

$$\delta\nu \simeq -\frac{\Delta\nu}{\pi} \delta\mathcal{F}. \quad (\text{A11})$$

From this we estimate that the range of the residual variation in ν with solar cycle, after removing the linear trend, is below $0.04 \mu\text{Hz}$, which apparently is substantially smaller than the variation in the signature of helium ionization inferred by Basu & Mandel (2004) and Verner et al. (2006). This deserves further investigation.